NEUROSCIENCE

An antidepressant mechanism underlying the allosteric inhibition of GluN2D-incorporated NMDA receptors at GABAergic interneurons

Jilin Zhang[1,2]†, Jinjin Duan[3,4]†, Wei Li[1,2]†, Xian Wang[5], Shimin Ren[5], Luyu Ye[2,3], Fang Liu[3], Xiaoting Tian[3], Yang Xie[3], Yiming Huang[1], Yidi Sun[1], Nan Song[1], Tianyu Li[2,3], Xiang Cai[6,7], Zhiqiang Liu[8], Hu Zhou[8], Chenggang Huang[3], Yang Li[3,5]*, Shujia Zhu[1,2,9]*, Fei Guo[3,8]*

***N*-methyl-D-aspartate receptors (NMDARs), key excitatory ion channels, have gained attention as anti-depression targets. NMDARs consist of two GluN1 and two GluN2 subunits (2A-2D), which determine their pharmacological properties. Few compounds selectively targeting GluN2 subunits with antidepressant effects have been identified. Here, we present YY-23, a compound that selectively inhibits GluN2C- or GluN2D-containing NMDARs. Cryo-EM analysis revealed that YY-23 binds to the transmembrane domain of the GluN2D subunit. YY-23 primarily affects GluN2D-containing NMDARs on GABAergic interneurons in the prefrontal cortex, suppressing GABAergic neurotransmission and enhancing excitatory transmission. Behavioral assays demonstrate YY-23's rapid antidepressant effects in both stress-naïve and stress-exposed models, which are lost in mice with global or selective knockout of the *grin2d* gene in parvalbumin-positive interneurons. These findings highlight GluN2D-containing NMDARs on GABAergic interneurons as potential depression treatment targets.**

INTRODUCTION

Major depressive disorder (MDD) is one of the most common psychiatric diseases (*1*). After decades of preclinical and clinical research, the neurobiological basis and aetiological mechanism of MDD remain elusive, probably due to the heterogeneous genetic and environmental correlates, the lack of potential biomarkers, and the scarcity of representative animal models. Most clinically available antidepressants developed on the basis of the classic monoaminergic theory produce low remission rates with long response lag times, moderate pharmacotherapeutic efficacy, and high individual heterogeneity (*2*). Thus, there is an urgent need for the development of faster-acting and more efficacious therapeutic agents to treat patients with MDD, especially those who are refractory to conventional antidepressants.

In recent years, a wealth of compelling studies has suggested that impairment of the glutamatergic system is likely to underlie the pathophysiology of depression (*3*, *4*). This accumulating evidence has come mainly from studies of the rapid-acting antidepressant ketamine, which is an *N*-methyl-D-aspartate receptor (NMDAR) channel blocker (*5*–*8*). It has been suggested that ketamine treatment enhanced glutamate transmission in the prefrontal cortex (PFC) and hippocampus in rodents and humans by blocking NMDA receptors (NMDARs) on GABAergic interneurons (*9*, *10*). This process instantly triggers dendritic spine regrowth (*11*) and cortical excitability (*6*, *7*). As a result, NMDAR antagonism has received much attention as a theory for the development of rapid-acting antidepressants.

NMDARs are glycine and glutamate coactivated ion channels involved in synaptic neurotransmission and plasticity in the vertebrate brain (*12*). Typical NMDARs are composed of two obligatory GluN1 subunits bound to glycine and two alternative GluN2 subunits (types 2A, 2B, 2C, and 2D) bound to glutamate, forming either diheteromeric or triheteromeric tetramers. The four GluN2 subunits display distinct temporal and spatial expression patterns and contribute to various biophysical and pharmacological properties of NMDARs (*13*, *14*). Notably, cell type–specific NMDAR subtypes have been approved as molecular targets for the antidepressant action of ketamine and rapastinel; the latter is a positive allosteric modulator (PAM) of NMDARs (*15*). GluN2A/2B-containing NMDARs are the predominant subtypes expressed in the adult brain, whereas GluN2C/2D-containing NMDARs are specifically confined to discrete regions that play a crucial role in disease pathology. For example, in schizophrenia, recent evidence has highlighted the critical role of NMDAR hypofunction in cortical GABAergic neurons, particularly where GluN2D subunits are prominently expressed (*16*, *17*). Notably, ketamine exhibited slightly higher potency for GluN2D than GluN2A and GluN2B (*18*), and a study suggests that GluN2D subunit is critical for the sustained antidepressant effects of (R)-ketamine (*19*). Although inhibiting GluN2D-containing NMDAR has been proposed as a potential strategy to treat depression, the druggability of it remained elusive.

Our previous study identified a compound named YY-23 that selectively inhibited the activity of NMDARs but not AMPA receptors (AMPARs) in cultured hippocampal neurons (*20*, *21*). In this study, we aimed to assess whether YY-23–mediated inhibition of NMDARs displays subtype selectivity and to understand the molecular mechanism underlying its fast antidepressant effects in vivo. Here, we show

[1]Institute of Neuroscience, CAS Center for Excellence in Brain Science and Intelligence Technology, Chinese Academy of Sciences, Shanghai 200031, China. [2]University of Chinese Academy of Sciences, No.19A Yuquan Road, Beijing 100049, China. [3]Key Laboratory of Receptor Research, Shanghai Institute of Materia Medica, Chinese Academy of Sciences, Shanghai 201203, China. [4]Shanghai YangZhi Rehabilitation Hospital (Shanghai Sunshine Rehabilitation Center), Frontier Science Center for Stem Cell Research, School of Life Sciences and Technology, Tongji University, Shanghai 200092, China. [5]School of Chinese Materia Medica, Nanjing University of Chinese Medicine, Nanjing 210003, China. [6]Oujiang Laboratory, Wenzhou Medical University, Wenzhou, Zhejiang 325000, China. [7]School of Mental Health, Wenzhou Medical University, Wenzhou, Zhejiang 325035, China. [8]Gynecology Hospital of Fudan University, No. 128, Shenyang Rd, Yangpu District, Shanghai 200082, China. [9]Shanghai Center for Brain Science and Brain-Inspired Intelligence Technology, Shanghai 201210, China.
*Corresponding author. Email: fguo877@126.com (F.G.); shujiazhu@ion.ac.cn (S.Z.); liyang@simm.ac.cn (Y.L.)
†These authors contributed equally to this work.

that YY-23 preferentially acts as an allosteric inhibitor for GluN2C- and GluN2D-containing NMDAR. Cryo-electron microscopy (cryo-EM) structures of GluN2D- containing NMDAR were identified in complex with YY-23, providing structural evidence of on-target binding of YY-23 at the molecular level. We found that YY-23 produced fast-onset antidepressant actions on various animal models of depression. Electrophysiological recordings and behavior studies on transgenic animals further demonstrated that the GluN2D subunit on GABAergic interneurons in the medial prefrontal cortex (mPFC) played a pivotal role in mediating the antidepressant effects of YY-23.

RESULTS

YY-23 selectively inhibits GluN2C- or GluN2D-containing NMDARs

As described in our previous report (*22*), YY-23 was obtained by acid hydrolysis of timosaponin B3 or chemical synthesis from timosaponin B2 (fig. S1 and table S1). YY-23 was isolated as a white amorphous powder, $[\alpha]_D^{20}$ − 66.0 (c 0.05, pyridine), with a molecular formula of $C_{33}H_{54}O_8$ as determined by positive-ion High-Resolution (HR)–electrospray ionization (ESI)–time-of-flight (TOF)–mass spectrometry (MS) (detected mass/charge ratio: 601.3713 [M + Na]+; calcd. For $C_{33}H_{54}O_8Na$: 601.3711). The ^{13}C–nuclear magnetic resonance (NMR) spectrum and distortionless enhancement by polarization transfer experiment showed the presence of 4 methyl groups, 12 methylene groups, 13 methine groups, and 4 quaternary carbons. The presence of a β-glycopyranosyl moiety was determined by the anomeric proton at δ_H 4.87 (J = 7.7 Hz) and the carbon signal at δ_C 105.19. The NMR spectral data of YY-23 were very similar to those of timosaponin BIII, indicating that the two have the same basic skeleton. In the heteronuclear multiple-bond correlation spectra, long-range correlations were observed from δ_H 4.87 (H-1′) to δ_C 75.22 (C-26) and vice versa. Accordingly, the structure of YY-23 was elucidated and named (25S)-3,26-dihydroxy-20(22)-ene-5β-furost-26-β-D-glucopyranoside (Fig. 1A).

We first investigated whether this compound targets monoaminergic receptors. FLIPR Calcium 4 Assay Kits were used to screen the $5HT_{2A}$, $5HT_{2B}$, and $5HT_{2C}$ serotonin receptors, while Lance Ultra cAMP Kits were used to screen the $5HT_{1A,}$ D_1R, D_2R, and D_4R dopamine receptors. When YY-23 was applicated (starting at 100 μM with 3× serial dilutions), it exhibited no notable effects on these receptors, indicating that YY-23 has negligible activity on these monoamine receptors (table S2). For instance, YY-23 at 10 μM (and potentially higher concentrations) did not show noticeable activation or inhibition of these receptors (Fig. 1, B and C). We also conducted a functional evaluation of YY-23 on the dopamine transporter (DAT), serotonin transporter (SERT), and the α7 nicotinic acetylcholine receptor. The results demonstrated that YY-23 had no meaningful inhibitory activity on DAT and SERT (fig. S2, A and B), while it exhibited only a weak inhibitory effect on the α7 receptor (fig. S2C). These findings suggest that monoaminergic receptors are unlikely to be the primary targets of YY-23.

On the basis of our previous data, YY-23 selectively inhibits NMDA- but not AMPA-induced currents in cultured hippocampal neurons (*21*). We next investigated whether YY-23–mediated inhibition displays subtype specificity by performing electrophysiological recordings on recombinant GluN1-GluN2 receptor subtypes expressed in either *Xenopus laevis* oocytes or human embryonic kidney (HEK) 293T cells. We found that YY-23 selectively reduced the glycine- and glutamate-induced maximal responses of GluN1-GluN2C and GluN1-GluN2D NMDARs (Fig. 1, D to G; fig. S3, A and B; and table S3). We noticed that the inhibitory effect of YY-23 on GluN1-GluN2D receptor expressed in *Xenopus* oocytes was difficult to reach the plateau until 10 min of application (fig. S3, A and B). In contrast, YY-23 had minimal effects on both GluN1-GluN2A and GluN1-GluN2B receptors (Fig. 1, D to G).

YY-23 acts as an allosteric inhibitor binding to the GluN2 transmembrane domain

Next, we examined the effect of YY-23 on the current-voltage (*I-V*) relationship of GluN1a-GluN2D receptors. In contrast to the conventional voltage-dependent magnesium block, the *I-V* curve exhibited a voltage-independent profile upon application of 10 μM YY-23 (Fig. 1H). There was no significant difference in the inhibition level when the holding potential was set to −60, −40, or +40 mV (Fig. 1I). To elucidate whether YY-23–mediated inhibition relies on the gating states of GluN1-GluN2D receptors, we applied 10 μM YY-23 to the nonactivated receptors for the same duration as for the activated receptors. The results showed that YY-23 also bound to GluN1-GluN2D receptors in the apo state and displayed a remarkable inhibitory effect (Fig. 1J). We then examined YY-23–mediated inhibition at various concentrations of glycine or glutamate and found that the inhibition occurred in an agonist concentration-independent manner (Fig. 1K). On the basis of this evidence, we proposed that YY-23 acts as an allosteric inhibitor to GluN1-GluN2D receptors.

Next, we tried to identify structural elements in NMDARs that might be responsible for the action of YY-23. GluN1 and GluN2 subunits share similar topological architectures, with two tandem extracellular domains comprising an N-terminal domain (NTD) and a ligand binding domain (LBD), a transmembrane domain (TMD) where the ion channel is located, and an intracellular C-terminal domain (CTD) (Fig. 2A) (*12*). Both the NTD and LBD have a bi-lobed clamshell-like architecture, and the LBD is composed of S1 and S2 segments linked with TMD helices (Fig. 2A). We first constructed truncated or chimeric subunits to search for the structural elements involved in YY-23–mediated inhibition (Fig. 2, A and B). Two electrode voltage-clamp (TEVC) recordings showed that the chimeric GluN1-GluN2D receptors with replacement of either NTD, NTD plus linker, or the S1 portion of the GluN2D subunit with that of the GluN2A subunit, as well as with the CTD deleted GluN1-GluN2D receptors, displayed YY-23 inhibition similar to that of wild-type (WT) GluN1-GluN2D receptors (Fig. 2B). Notably, GluN1-GluN2D (2A-S2) and GluN1-GluN2D (2B-S2) receptors showed a partial reduction in the inhibitory effect of YY-23 (Fig. 2, B and C). More notably, GluN1-GluN2A (2D-S2) or GluN1-GluN2B (2D-S2) receptors displayed a substantial gain of function of YY-23–mediated inhibition (Fig. 2, B and C). Together, these data demonstrate that the S2 region of the GluN2D subunit is critical for the allosteric action of YY-23.

To determine the YY-23 binding site on GluN1-GluN2D receptors, we carried out a cryo-EM experiment on the human GluN1b-GluN2D receptor with the CTD deleted and in the presence of the agonist glycine, the competitive antagonist (*R*)-4-(3-phosphonopropyl) piperazine-2-carboxylic acid (*R*-CPP) and YY-23. We confirmed that the inhibitory effect of YY-23 was also observed for GluN1b-GluN2D receptors (fig. S3B). Next, we resolved the cryo-EM structure of YY-23–bound GluN1b-GluN2D receptors at the resolution of 4.2 Å (Fig. 2D; fig. S3, C to F, and table. S4). After modeling the GluN1b and

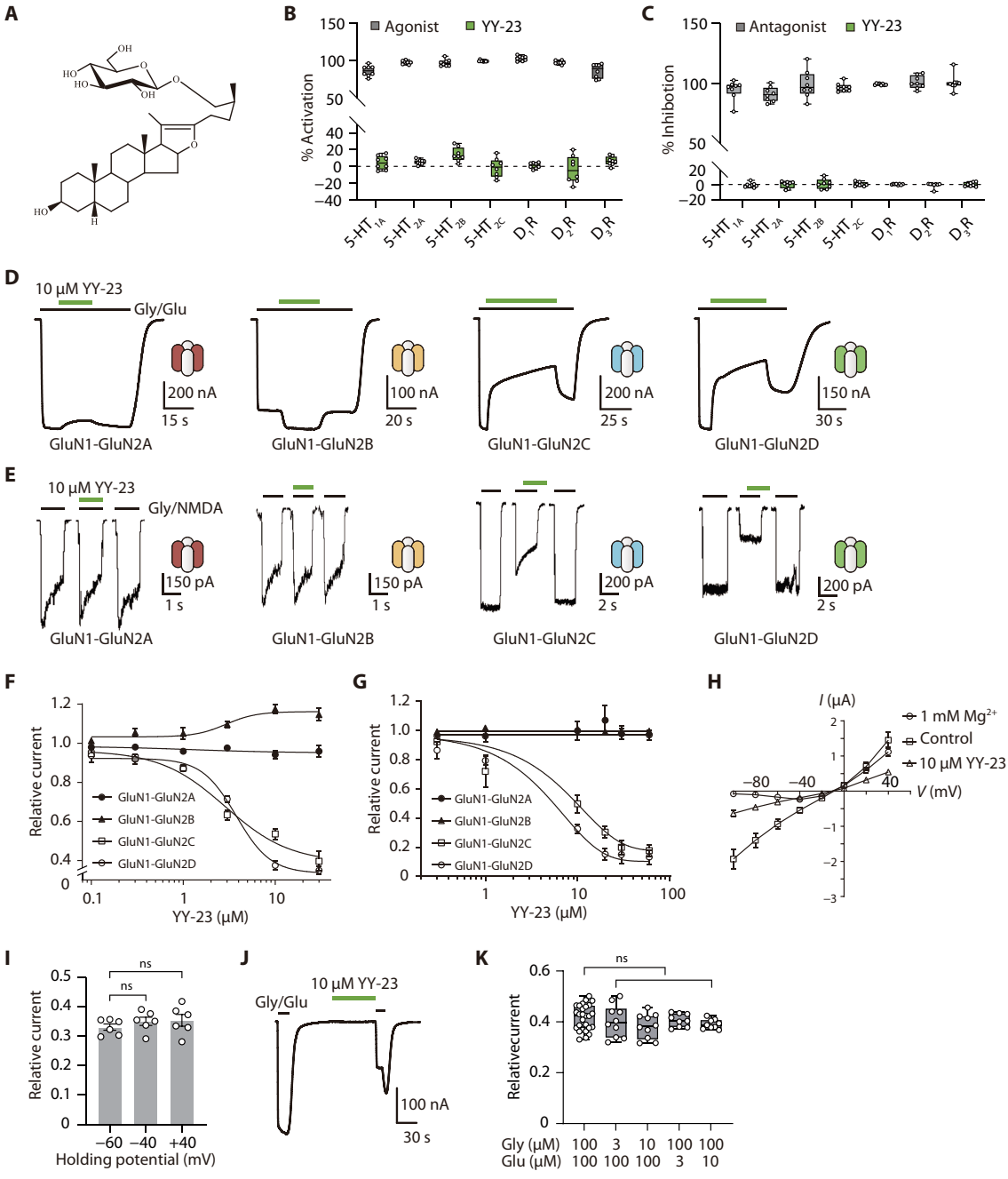

Fig. 1. Specificity of YY-23 action on NMDAR subtypes. (**A**) Chemical structure of YY-23. (**B** and **C**) Effects of YY-23 on $5HT_{1A}$, $5HT_2B$, and $5HT_2C$ receptors (FLIPR Calcium 4 Assay) and $5HT_{2A}$, D_1R, D_2R, and D_4R in both agonist and antagonist modes. Data were processed using an unpaired *t* test for normally distributed data and the Mann-Whitney test for nonnormally distributed data. (**D** and **E**) Representative current traces from recombinant NMDARs in *Xenopus* oocytes [(D), TEVC] with 100 μM glutamate, 100 μM glycine, and 10 μM YY-23 and from HEK293T cells [(E), whole-cell voltage-clamp] with 500 μM NMDA, 20 μM glycine, and 10 μM YY-23. (**F** and **G**) Concentration-response curves showing the effect of YY-23 on NMDARs in *Xenopus* oocytes (mean ± SD) and HEK293T cells (mean ± SEM). (**H**) Current-voltage (*I-V*) relationships for GluN1-GluN2D receptors with control (squares), 10 μM YY-23 (triangles), or 1 mM $Mg2^+$ (circles) in the presence of saturating glycine and glutamate (100 μM each). (**I**) Statistical analysis of YY-23–mediated inhibition at holding potentials of −60, −40, and +40 mV. (**J**) Representative trace depicting the GluN1-GluN2D receptor response to a 1-min exposure to 10 μM YY-23 without agonists. (**K**) Inhibition efficacy of YY-23 on GluN1-GluN2D receptors at varying concentrations of glycine and glutamate, normalized to currents induced by 100 μM glycine and glutamate. (I) and (K) were analyzed by one-way analysis of variance (ANOVA). ns, not significant.

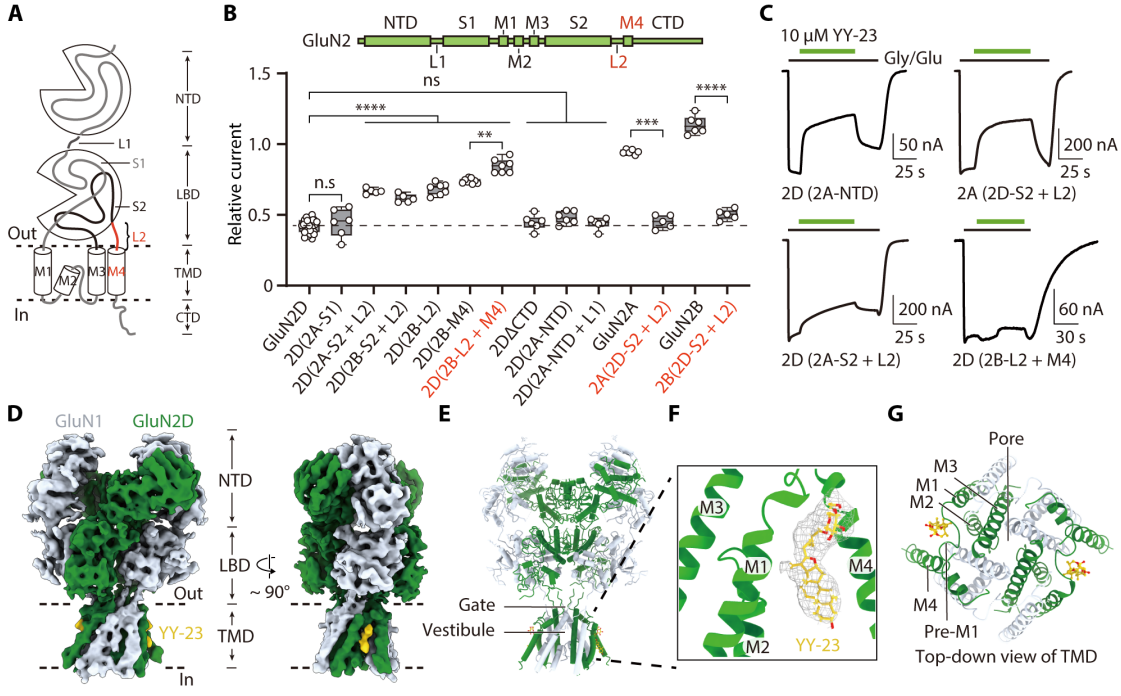

Fig. 2. Structural determinants of YY-23 inhibition. (**A**) Topological structure of GluN subunits showing NTD, LBD with S1 and S2 portions, TMD, and intracellular CTD. L1 and L2 are linkers connecting NTD-LBD and S2-M4, respectively. (**B**) Effects of 10 μM YY-23 on WT, chimeric, and truncated receptors in *Xenopus* oocytes. Top shows a linear representation for a GluN2 subunit corresponding to the topological structure in (A). Dashed line aligned with the media response of the GluN1-GluN2D WT receptor provides a benchmark for the YY-23–mediated inhibitory effect. Data were analyzed by Brown-Forsythe ANOVA with Dunnett's T3 post hoc. Individual cells are represented by data points. Mean ± SEM are shown in bar graphs; box plots display minimum/maximum values, quartiles, and medians. Significance: "ns" ($P > 0.05$), $^{**}P < 0.01$, $^{***}P < 0.001$, and $^{****}P < 0.0001$. (**C**) Current traces of chimeric receptors responding to 10 μM YY-23 with saturating concentrations (100 μM) of glycine and glutamate ("Gly/Glu"). (**D**) Electron density map of GluN1b-GluN2D receptor bound with YY-23 (yellow). (**E**) Structure of YY-23 bound to GluN1-GluN2D receptor. (**F**) Detailed view of YY-23 density (mesh) within the binding site constituted by the M1, M2, and M4 helices of GluN2D subunit. (**G**) Top-down view of the TMD of GluN1b-GluN2D receptor with YY-23 bound.

GluN2D into the density by rigid-body fitting based on the structure of the *R*-CPP–bound GluN1a-GluN2D receptor [Protein Data Bank (PDB): 7YFF (*23*)], we identified a clear electron density in the TMD of the GluN2D subunit, which fitted well with the YY-23 molecule (Fig. 2, D and E). YY-23 inserted into a niche formed by the M1, M2, and M4 helices of GluN2D subunit, with its steroid moiety inserted in the pocket and sugar moiety extended outward (Fig. 2, F and G). To confirm the structural observation, we first verified whether residues among GluN2 subunits of the TMD region were directly responsible for YY-23 binding. We individually substituted all nonconserved residues in the TMD of GluN2D with their homologous residues in the GluN2A subunit. However, none of the mutant constructs led to a loss-of-function effect of YY-23 (fig. S4, A and B). Since YY-23 bound in the TMD of GluN2D and showed loss of function on chimeric GluN1-GluN2D (2B-S2) receptors, we proposed that the conformation of the S2-M4 linker and M4 may control the subtype-specific inhibitory effect of YY-23. Therefore, we generated chimeric constructs of GluN2D by replacing the S2-M4 linker and/or the M4 helix with the corresponding segments from the GluN2B subunit (Fig. 2, A and B). Substitution of either the S2-M4 linker or M4 resulted in a substantial decline of the YY-23 inhibition on GluN1-GluN2D receptor (Fig. 2B). Moreover, substitution of the S2-M4 linker together with the M4 segment completely abolished the YY-23 inhibition on GluN1-GluN2D receptors (Fig. 2, B and C). This evidence suggests that the S2-M4 linker and the M4 helix in GluN2D subunit are responsible for the subunit-selective YY-23 inhibition. In sum, these data provide structural evidence for a binding site within the TMD of the GluN2 subunit and elucidate the molecular basis of GluN2-dependent allosteric inhibition by YY-23.

YY-23 inhibits native GluN2D-containing NMDARs in the mPFC

The GluN2C subunit is dominantly expressed in the cerebellum, so we first chose GluN2D for the following in vivo studies, because it is widely distributed in the brain (*24*) and is closely associated with depression and anxiety (*19*, *25*). However, very little is known about the cell type–specific expression and functional role of the GluN2D subunit in the adult cortex. We performed multiplex fluorescence in situ hybridization (FISH) to examine *grin2d* mRNA expression in interneurons and pyramidal neurons in adult mice at 8 weeks (Fig. 3, A to D). We found that *grin2d* preferentially colocalized with cells positive for *slc32a1* (encoding GAD67) rather than those positive for *slc17a7* (encoding Vglut1). Transcriptomic analysis of NMDAR subunits using a single-cell RNA sequencing dataset (fig. S5) demonstrated that *grin1*, *grin2a*, and *grin2b* were densely expressed both in the inhibitory interneurons and excitatory neurons, whereas *grin2d* was preferentially expressed in the inhibitory neurons. These results confirmed that the GluN2D subunit was expressed in the mPFC in adult mice and preferentially colocalized with interneurons rather than pyramidal neurons.

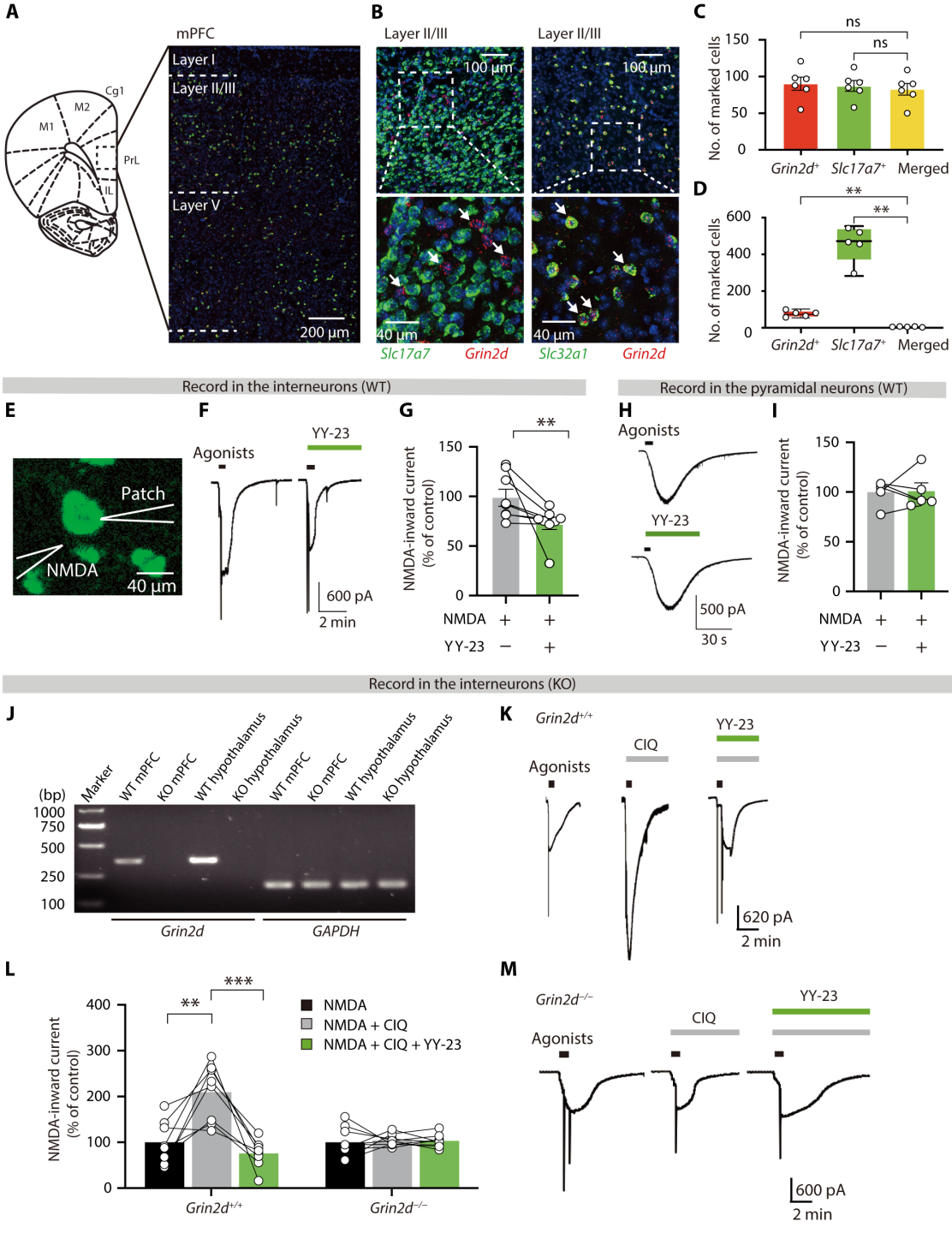

Fig. 3. YY-23 inhibits activity of interneurons via GluN2D subunit. (**A**) Coronal mouse brain section showing mPFC (dashed box), with confocal imaging of DNA (4′,6-diamidino-2-phenylindole, blue), grin2d mRNA (red), and *Slc32a1* mRNA (green) using multiplex FISH. Dashed lines indicate mPFC layers. PrL; prelimbic cortex; IL, infralimbic cortex; Cg1, cerebral cortex, area 1. (**B**) Localization of Sic17a7 (pyramidal neurons, green), *Slc32a1* (interneurons, green), and grin2d (red), with magnified views. Arrows highlight grin2d-positive neurons. (**C** and **D**) Quantification of single or dual mRNA-positive cells. Data were analyzed using one-way ANOVA for normally distributed data (C) and Brown-Forsythe ANOVA with Dunnett's T3 multiple comparisons for data with heterogeneous variance (D). (**E**) Patch-clamp setup from GAD67-GFP–positive mPFC slices. (**F** to **I**) NMDA-induced currents with/without 20 μM YY-23 in interneurons [(F) and (G)] and pyramidal neurons [(H) and (I)] from WT mice. Representative traces shown. Wilcoxon test for paired comparisons. (**J**) Quantitative PCR of mRNA in WT and grin2d knockout (KO) mice. (**K** and **L**) NMDA currents with 20 μM YY-23 and/or 3 μM CIQ in interneurons from WT and grin2d KO mice. Representative traces shown. [(K) and (L)] Representative recording traces. Data underwent one-way ANOVA and Tukey's multiple comparisons for histograms (**M**). Each point denotes an individual cell. Bar graphs represent mean ± SEM. Box plots depict min/max values, quartiles, and median lines. Significance: ns ($P > 0.05$), $^{**}P < 0.01$, and $^{***}P < 0.001$.

Next, we hypothesized that YY-23 may preferentially act on GluN2D-containing NMDARs and investigated the effects of YY-23 on NMDAR activity of layer II/III interneurons and pyramidal neurons in adult mPFC slices. NMDA-evoked inward currents from glutamate decarboxylase 1 (GAD67)–enhanced green fluorescent protein (EGFP)–labeled interneurons and pyramidal neurons were recorded by patch-clamp (Fig. 3E). We found that YY-23 markedly inhibited NMDA-evoked currents in interneurons (Fig. 3, F and G) but not in pyramidal neurons (Fig. 3, H and I). To further investigate whether YY-23 acted selectively on native GluN2D-containing NMDARs, we applied the selective allosteric potentiator CIQ to boost the currents of GluN2D-containing NMDAR currents (*26*). We found that YY-23 substantially blocked the enhancement of NMDA-evoked currents potentiated by 3 μM CIQ (Fig. 3, K and M). However, in *grin2d*-knockout (KO) mice [authenticated by quantitative polymerase chain reaction (PCR); Fig. 3J], neither CIQ nor YY-23 had any effect on NMDA-evoked currents (Fig. 3, L and M). These results suggest that YY-23 selectively blocks the GluN2D subunit–mediated inward current in mPFC interneurons.

Inhibition of GluN2D-containing NMDARs on GABAergic interneurons enhances excitatory transmission

To test the YY-23 neurotransmission on mPFC interneurons, we first recorded action potentials (APs) by a series of current injections in mPFC GAD67-EGFP–positive interneurons (Fig. 4, A to C). The numbers of APs were substantially reduced by YY-23 at concentrations of 1, 10, and 30 μM in a concentration-dependent manner (Fig. 4, B, D, and E). Given that YY-23 weakened the excitability and firing output of interneurons, we wondered how these changes might affect the inhibitory output onto nearby pyramidal neurons. Thus, we compared spontaneous inhibitory postsynaptic currents (sIPSCs) in mPFC layer V pyramidal neurons in WT and KO mice. YY-23 at 10 μM reduced the frequency but not the amplitude of sIPSC in WT mice (Fig. 4, F to M). This was also observed in the miniature inhibitory postsynaptic currents (mIPSCs) recorded from the pyramidal neurons (fig. S6, A to H). The results indicate that the GABAergic output from interneurons to pyramidal neurons was inhibited. As sIPSC makes postsynaptic more likely to inhibit firing of AP, we then examined whether this inhibition affected the excitability of pyramidal neurons. The results showed that YY-23 (10 μM) increased the number of APs (Fig. 4, N to Q) and the frequency and amplitude of miniature EPSC (mEPSC) (fig. S6, I to Q), suggesting that YY-23 may enhance the excitability of pyramidal neurons by disinhibiting the GABAergic output of interneurons. Furthermore, we found that YY-23–induced inhibition of sIPSC and enhancement of AP in pyramidal neurons were prevented in the *grin2d* KO mice (Fig. 4, I and J to M), suggesting that the GluN2D subunit may contribute to the YY-23–induced reduction of inhibitory output onto nearby pyramidal neurons and enhancement of excitability of pyramidal neurons.

Given that the selective serotonin reuptake inhibitor (SSRI) fluoxetine altered neither the mEPSC frequency (fig. S7, A to F) nor the amplitude (fig. S7, G to I) in pyramidal cells suggested a unique neuropharmacological mechanism of YY-23 compared with SSRIs. The results suggested that YY-23 directly inhibits GluN2D-containing NMDARs within interneurons, which reduces the inhibitory output of GABAergic interneurons and in turn results in the disinhibition of pyramidal cells. Thus, we speculate that the fast antidepressant effect of YY-23 is likely to be related to the induced enhancement of excitatory synaptic transmission in the mPFC in a characteristic manner involving disinhibition.

The antidepressant properties of YY-23

To investigate the antidepressant characteristics of YY-23, we first optimized its dosage using naïve mice. YY-23 was administered acutely, 30 min before behavioral tests. In the novelty-suppressed feeding test and the forced swimming test (FST), YY-23 notably decreased feeding latency and immobility time in a dose-dependent manner (Fig. 5, A and B). There were no significant changes in the total distance traveled during the open field test (OFT), indicating that YY-23 did not affect locomotor activity (Fig. 5C). These findings confirm that YY-23 exhibits clear antidepressant-like effects upon acute administration.

We then used a chronic social defeat stress (CSDS) model in mice (*27*) to assess whether YY-23 could prevent stress-induced depressive symptoms (Fig. 5, D to F). Mice were classified on the basis of their social interaction (SI) ratio of 1, indicating equal time spent with and without a social target (CD-1). Mice with an SI ratio below this threshold were deemed susceptible. After 10 days of CSDS, about 60% of the stressed mice showed a defeated phenotype, characterized by reduced interaction zone time (Fig. 5F). Susceptible mice were then assigned to receive either a vehicle, YY-23 (10 mg/kg), or fluoxetine (10 mg/kg). Depressive-like symptoms were evaluated using the sucrose preference test (SPT) and the tail suspension test (TST) (Fig. 5D), conducted 24 hours after the SI test on days 8 and 15, respectively.

Following 1 week of daily YY-23 administration, susceptible mice displayed a recovery in interaction zone time, similar to control mice, suggesting reversal of depressive symptoms. In contrast, 3 weeks of fluoxetine treatment did not reverse social defeat behavior (Fig. 5E). In addition, YY-23 administration alleviated increased immobility in the TST (Fig. 5G) and decreased sucrose consumption in the SPT (Fig. 5H), indicating a reversal of depressive-like symptoms. YY-23–treated mice showed normal locomotor activity compared to controls (Fig. 5I).

The antidepressant effects of YY-23 were further confirmed in a corticosterone-induced depression model, characterized by hypothalamic-pituitary-adrenal hyperactivity from 21 days of corticosterone supplementation (Fig. 5J). Depressive symptoms were assessed using the SPT and FST. Corticosterone-exposed mice exhibited reduced sucrose preference and increased immobility time, which were ameliorated by a single oral dose of YY-23 (Fig. 5, K and L). Similarly, (S)-ketamine improved sucrose preference and reduced immobility time (Fig. 5, K and L). Overall, YY-23 effectively reversed depressive phenotypes induced by CSDS and corticosterone, demonstrating rapid antidepressant action.

GluN2D subunit in PV interneurons is crucial for antidepressant efficacy of YY-23

To determine whether GluN2D-containing NMDARs are essential for YY-23's antidepressant effects, we used GluN2D KO ($grin2d^{-/-}$) and heterozygous ($grin2d^{+/-}$) mice. In the FST and TST (Fig. 6, A and B), YY-23 substantially reduced immobility time in WT mice compared to vehicle-treated controls. However, this effect was absent in $grin2d^{-/-}$ and $grin2d^{+/-}$ mice. The distance traveled in the locomotor test did not differ among $grin2d^{+/+}$, $grin2d^{+/-}$, and $grin2d^{-/-}$ groups (Fig. 6C), suggesting that YY-23's antidepressant-like effects are not due to increased locomotion. The absence of the GluN2D

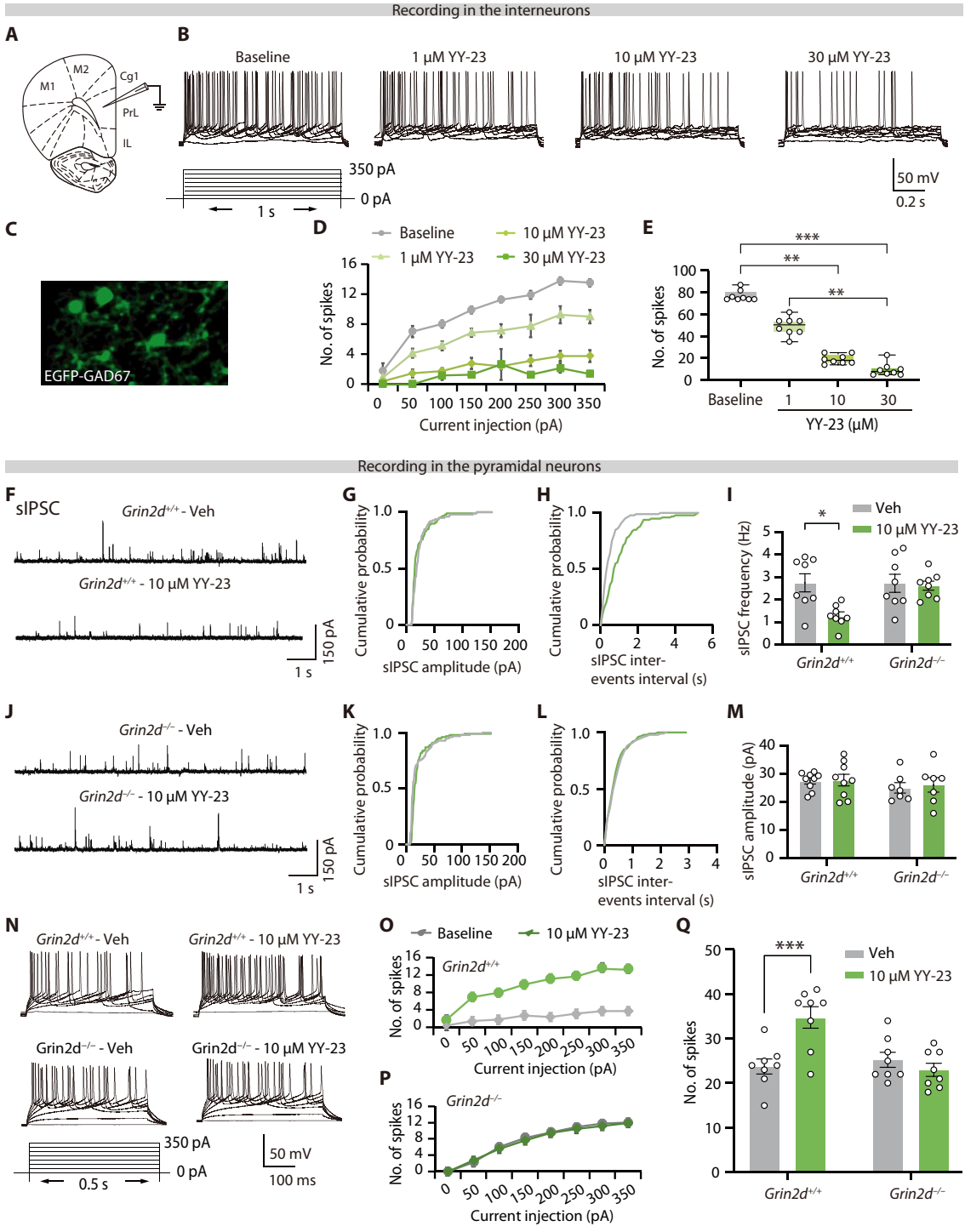

Fig. 4. YY-23 up-regulated activity of pyramidal neuron by inhibiting interneuron. (**A**) Coronal mouse brain section showing electrode placement in the prelimbic area (PrL). (**B** and **C**) Active potential recordings (B) from GAD67-EGFP–positive interneurons (C) in the mPFC. (**D** and **E**) Spike counts from graded current injections (0 to 350 pA in 50-pA steps) on interneurons with varying YY-23 concentrations (D). Data analyzed by Kruskal-Wallis ANOVA and Dunn's post hoc test. Box plots show min/max values, quartiles, and medians (E). (**F** to **K**) sIPSC recordings in mPFC pyramidal neurons from WT and *grin2d*$^{-/-}$ mice, before and after 10 μM YY-23. Cumulative distributions of sIPSC intervals [(H) and (K)] and frequencies [(G) and (J)] analyzed by Kolmogorov-Smirnov test. (**L** and **M**) Bar graphs comparing sIPSC frequencies (L) and amplitudes (M) at baseline (gray) and post–YY-23 (green) in WT and *grin2d*$^{-/-}$ mice, analyzed by repeated measures (RM) two-way ANOVA with Bonferroni's post hoc test. (**N**) AP recordings in pyramidal neurons with YY-23 in WT versus *grin2d*$^{-/-}$ mice. (**O** and **P**) Spike frequency response to current injections in pyramidal neurons with YY-23 in WT (O) and *grin2d*$^{-/-}$ mice (P). (**Q**) Average spike counts pre– and post–YY-23 in WT and *grin2d*$^{-/-}$ mice, analyzed by RM two-way ANOVA with Bonferroni's test. Bar graphs show mean ± SEM. Significance: $*P < 0.05$, $**P < 0.01$, and $***P < 0.001$.

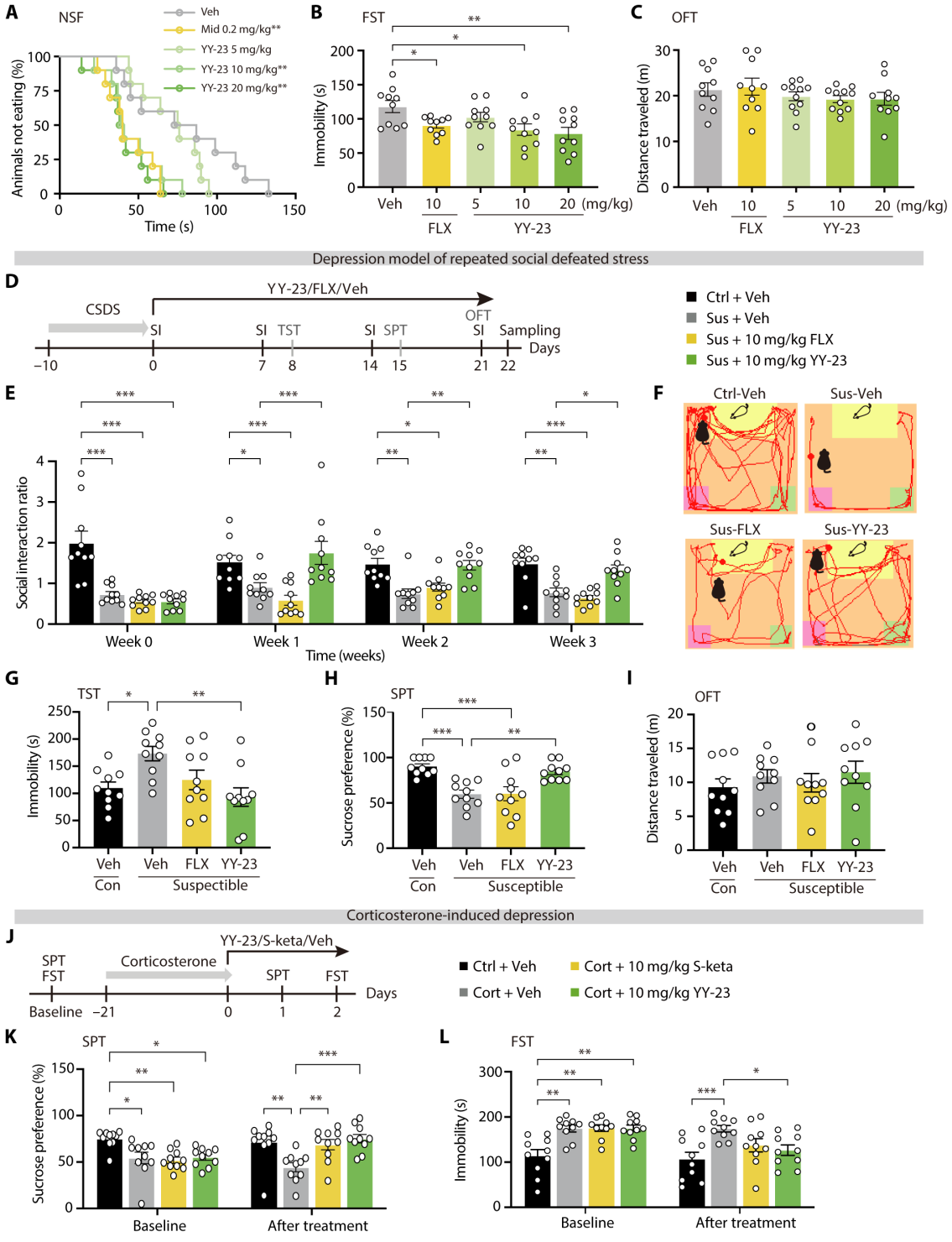

Fig. 5. Rapid antidepressant effect of YY-23 on mice. (**A** to **C**) YY-23 shows dose-dependent antidepressant-like effects in stress-naïve mice, as measured by the novelty-suppressed feeding test (A) and forced swimming test (B). No impact on locomotion was observed in the OFT (C). Data analyzed by Kaplan-Meier survival analysis with Mantel-Cox test (A) and one-way ANOVA with Dunn's correction [(B) and (C)]. (**D**) Experimental timeline for behavioral tests, drug administration, and brain tissue collection in a CSDS model. Mice received treatments of vehicle, fluoxetine (FLX), or YY-23 after 10 days of social stress, with tissue collected 24 hours after the final dose. (**E**) Social interaction (SI) ratio for each group weekly, analyzed by repeated measures (RM) two-way ANOVA with Tukey's test. (**F**) Exploratory trajectories of C57BL/6N mice with 21 days of drug administration. Yellow box shows the SI zone. "Sus" indicates susceptible mice. (**G** to **I**) TST (G), SPT (H), and OFT (I) were assessed, and data were analyzed by one-way ANOVA with Tukey's test. (**J** to **L**) Overview and effects of YY-23 and (S)-ketamine in a corticosterone-induced depressive model. SPT (K) and FST (L) data analyzed by RM two-way ANOVA with Tukey's test. Bar graphs represent mean ± SEM. Significance: $*P < 0.05$, $**P < 0.01$, and $***P < 0.001$.

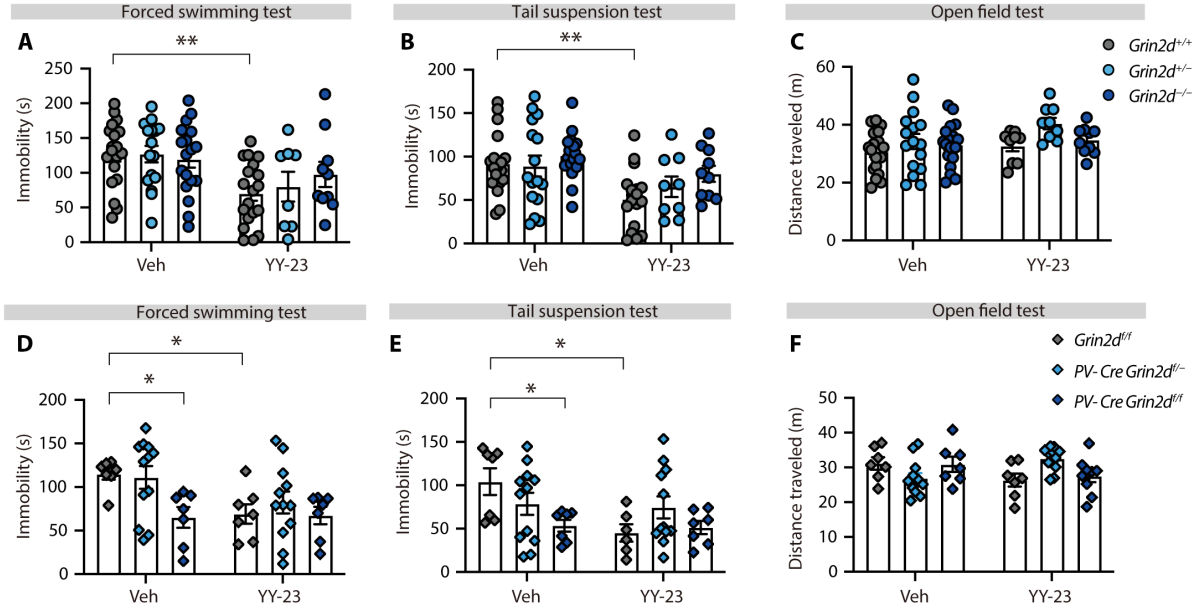

Fig. 6. Genetic deletion of *grin2d* abolished the antidepressant-like effect of YY-23. (**A** to **C**) YY-23 reduced immobility time in the FST (A) and TST (B) in WT (*grin2d*$^{+/+}$) mice but not in grin2d KOs (*grin2d*$^{+/-}$ and *grin2d*$^{-/-}$), indicating the need for the grin2d gene for YY-23's effects. No changes in locomotion were observed in the OFT (C). (**D** to **F**) Behavioral effects of YY-23 on mice with (PV-Cre *grin2d*$^{f/-}$ and PV-Cre *grin2d*$^{f/f}$) and without (*grin2d*$^{f/f}$) *grin2d* deletion in PV-positive interneurons. Data were analyzed by two-way ANOVA with Bonferroni correction. Bar graphs show means ± SEM. Significance: $^{*}P < 0.05$ and $^{**}P < 0.01$.

gene did not produce antidepressant effects, possibly because of a compensatory response in the body.

To address the potential involvement of GluN2C in the antidepressant effects of YY-23, we conducted additional experiments using *grin2c* KO mice (fig. S8A). With Western blot, we found almost no expression of GluN2C protein in the hippocampus and cerebral cortex but abundant GluN2C in cerebellum of adult mice (fig. S8A). Behavioral tests show that *grin2c* KO mice displayed hyperactivity in the OFT compared to control mice (fig. S8B). In addition, the immobility time in *grin2c* KO mice was not notably different from that of control mice in both the FST (fig. S8C) and the TST (fig. S8D). Therefore, the antidepressant-like effects of YY-23 (10 mg/kg) were not blocked in *grin 2c* KO mice, indicating that YY-23 likely targets the GluN2D subunit rather than the GluN2C subunit to exert its antidepressant effects.

Given the specific expression of GluN2D in parvalbumin (PV) interneurons, we hypothesized that selective deletion of GluN2D in these neurons would affect YY-23's efficacy. We crossed *grid 2d* loxp transgenic mice with PV-cre transgenic mice to generate a PV-Cre *grin2d*$^{f/f}$ line with selective *grin2d* gene deletion in PV interneurons. While PV-Cre *grin2d*$^{f/-}$ mice exhibited no notable changes, their PV-Cre *grin2d*$^{f/f}$ counterparts demonstrated substantially diminished immobility times in both the FST and the TST (Fig. 6, D and E), indicating an antidepressant-like phenotype. Administration of YY-23 failed to evoke antidepressant effects in PV-Cre *grin2d*$^{f/f}$ mice (Fig. 6, D and E), with locomotor activity remaining unaffected (Fig. 6F). These results underscore the critical role of the GluN2D subunit in PV interneurons for mediating the antidepressant effects of YY-23.

YY-23 reverses stress-induced proteomic changes in susceptible mice

To further investigate the pathophysiological mechanism underlying stress-induced depression and to identify the phenotype-specific molecular function of YY-23, we used quantitative proteomics to analyze protein expression in the mPFC. Three animals were used per group for brain tissue sampling 24 hours after 3 weeks of drug administration (Fig. 5D), and a total of 4915 distinct proteins were quantified by MS. Proteomic analysis revealed that the expression levels of 120 proteins were significantly different between the susceptible and control groups. Unsupervised hierarchical clustering analysis of these 120 proteins clustered them into four distinct groups representing the four different responses to the treatments (Fig. 7A). We also found that the changes in 26 altered proteins in the susceptible group (stress versus ctrl) were substantially reversed by YY-23 (YY-23 versus stress; Fig. 7B). Thus, these proteins represent some common components that are oppositely regulated by stress and YY-23. The clustering analysis results shown in the heatmap further revealed that the 26 proteins, including 11 proteins that were up-regulated and 15 that were down-regulated by stress, could be oppositely regulated by YY-23 (Fig. 7C). In contrast, fluoxetine, an antidepressant with a long response lag, rescued the levels of only 12 of the 120 proteins that were changed by stress (fig. S9).

To gain insight into the involvement of these proteins in different molecular and biological functions, Gene Ontology annotation of the 26 proteins inversely regulated by YY-23 was performed. Nine terms were substantially enriched in the molecular function category. The identified proteins were mainly involved in receptor internalization, response to calcium ions, and positive regulation of synaptic transmission (Fig. 7D).

Antidepressant effects of YY-23 depend on its promotion of synaptic plasticity

To further explore the synaptic modulation induced by YY-23, we recorded field excitatory postsynaptic potentials (fEPSPs) in the mPFC. The stimulating electrode was placed in layer V, and the

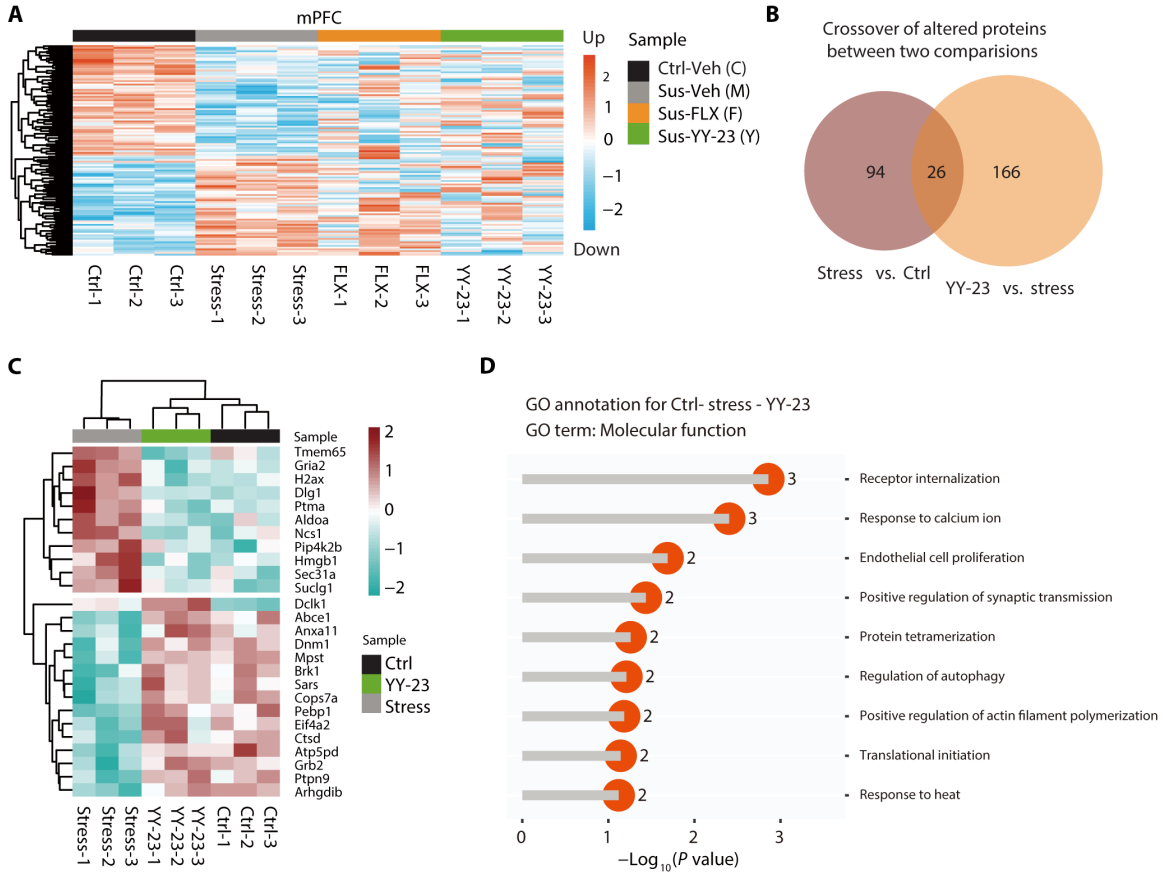

Fig. 7. YY-23 enhanced synaptic transmission based on proteomic analysis. (**A**) Clustering of differentially expressed proteins in the mPFC from control (Ctrl-Veh) and susceptible mice treated with vehicle, fluoxetine (10 mg/kg; Sus-FLX), or YY-23 (10 mg/kg; Sus-YY-23) ($n = 3$ per group). Sampling details are in Fig. 4D. (**B**) Venn diagram showing altered proteins in the stress group versus control and in the YY-23 group versus the stress group, with YY-23 rescuing 26 proteins. (**C**) Clustering of these 26 proteins indicating restoration by YY-23 in susceptible mice. (**D**) Gene Ontology (GO) enrichment analysis of the biological processes related to these proteins.

recording electrode in layer II/III (Fig. 8A). Unexpectedly, the initial slope of the fEPSP substantially increased within 10 min of YY-23 application, and this effect persisted for up to 40 min (Fig. 8B). The fEPSPs were inhibited by the application of the AMPAR antagonist CNQX, confirming their dependence on AMPARs. These results suggest a strong association between the identified proteins (Fig. 7) and synaptic transmission following YY-23 treatment.

We aimed to further investigate the mechanism underlying YY-23–induced enhancement of excitatory synaptic transmission. Previous studies have implicated the mammalian target of rapamycin (mTOR) signaling pathway, which is localized to dendrites and the cell body and regulates translation, in rapid antidepressant effects and long-term synaptogenesis (*28*, *29*). To examine the role of mTOR in synaptic transmission, we pretreated mPFC slices with the selective mTOR inhibitor rapamycin (5 μM) for 30 min and then reevaluated fEPSPs. The results showed that rapamycin pretreatment at 5 μM inhibited the YY-23–induced enhancement of fEPSPs (Fig. 8, C and D). These findings suggest that the enhancement of excitatory synaptic transmission by YY-23 may be dependent on the mTOR signaling pathway.

To further assess the role of mTOR in YY-23's antidepressant effects, rapamycin was locally infused into the mPFC. We found that administration of YY-23 (10 mg/kg) markedly reduced immobility time in the TST (Fig. 8E) for mice treated with dimethyl sulfoxide (DMSO) but not in those treated with rapamycin. Similarly, YY-23 improved the time spent in the open arms of DMSO-treated mice in the elevated plus maze (Fig. 8F) but had no notable effect in rapamycin-treated mice. These data indicate a strong involvement of the mTOR signaling pathway in the antidepressant effects induced by YY-23.

DISCUSSION

In this study, we discovered a timosaponin derivative, YY-23, with selective inhibition of GluN2C– and GluN2D–containing NMDARs. Cryo-EM structure analysis and electrophysiological recordings suggested that YY-23 does not directly block the channel gate or compete with agonist binding. Instead, it acts as a negative allosteric modulator of GluN1-GluN2D receptors. YY-23 demonstrated rapid antidepressant effects in mouse models, which were abolished in *grin2d*-KO mice and mice with *grin2d* gene deletion in PV interneurons. In the mPFC region of the mouse brain, GluN2D was primarily expressed in GABAergic interneurons. YY-23 directly inhibited native GluN2D-containing NMDAR currents in the mPFC, leading to a decrease in the output of GABAergic interneurons. This disinhibited the excitability of pyramidal cells and promoted synaptic plasticity.

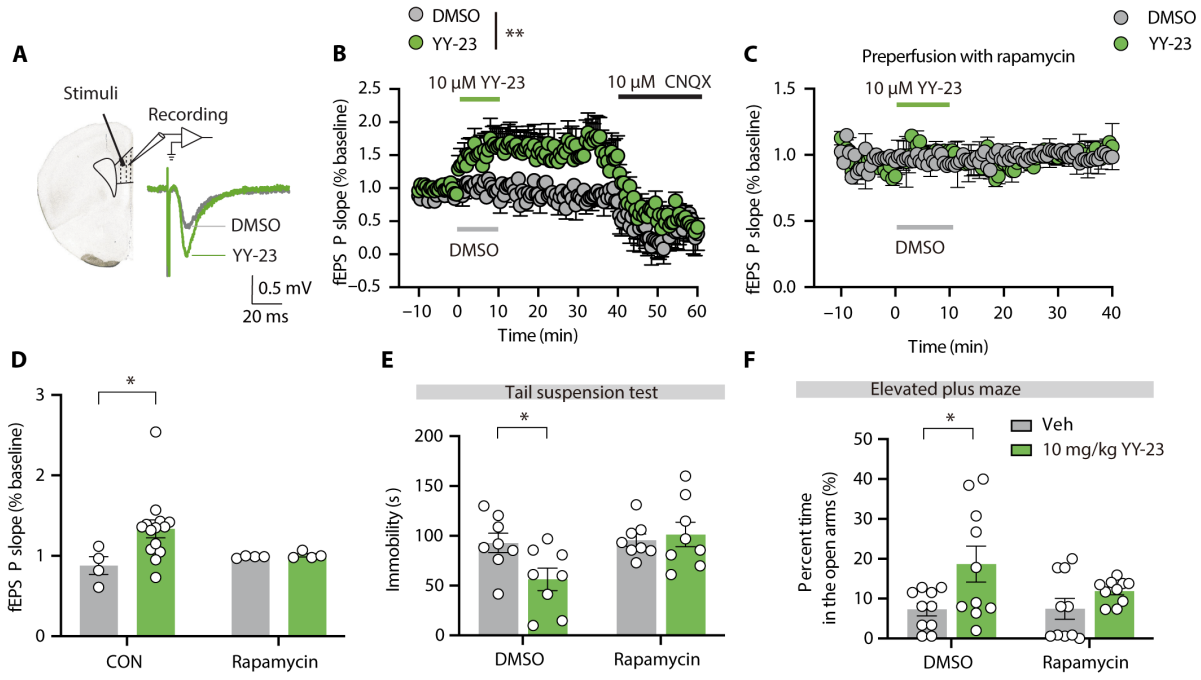

Fig. 8. YY-23 enhances LTP in mPFC, contributing to its antidepressant effect. (**A**) Schematic of fEPSP recording with stimulating electrode in layer VI and recording electrode in layer II/III; example traces are shown. (**B** and **C**) fEPSP slopes with (B) and without (C) rapamycin preperfusion. YY-23 and DMSO were administered at time zero (green line). CNQX was applied at 40 min to evaluate AMPAR involvement. Differences were analyzed using the Kolmogorov-Smirnov test. (**D**) YY-23 substantially increased fEPSP slope, an effect blocked by rapamycin preperfusion. (**E** and **F**) TST (E) and elevated plus maze (F) assessed the antidepressant-like effects of YY-23 in mice with 30-min preperfusion of DMSO or rapamycin in the PFC. Data [(D) to (F)] were analyzed by two-way ANOVA with Bonferroni post hoc test. Bar graphs show means ± SEM. Significance: $^{*}P < 0.05$ and $^{**}P < 0.01$.

GluN1-GluN2D receptors exhibit distinctive biophysical characteristics, including the highest agonist potency, the longest exponential deactivation time course, and the lowest channel open probability among NMDAR subtypes (*12*, *30*). Their activity can be modulated allosterically by endogenous protons (*31*); neurosteroids (*32*); and exogenous allosteric compounds, including CIQ 23, QNZ46 (*33*), and DQP-1105 (*34*). Allosteric modulators, which bind to sites distinct from the orthosteric agonist-binding sites (*35*), typically exert subunit-specific effects without altering fundamental channel function (*36*, *37*). For example, allosteric modulators like rapastinel often have fewer side effects compared to channel pore blockers like ketamine, which can induce psychotomimetic or dissociative effects (*38*). In this study, we identified a previously unreported allosteric modulator binding site composed of GluN2D Pre-M1, TM1, and TM4. These findings suggest that the TMD region of NMDARs holds promise as a target for the development of subtype-selective allosteric modulators.

Although both the antidepressant ketamine and YY-23 bind to the TMD of NMDARs, there are still some essential differences in their action mechanism. First, ketamine, along with PCP and MK-801, functions as a pore blocker in the vestibule, directly obstructing the ion influx pathway (*8*, *39*). In contrast, YY-23 acts as an allosteric inhibitor by binding to the periphery of the TMD in the GluN2D subunit. This binding inhibits the activity of NMDARs through an allosteric mechanism (Fig. 2). Second, ketamine shows voltage dependency and is ineffective during membrane depolarization (*40*, *41*), while the action of YY-23 is not influenced by voltage [see Fig. 1 (H and I)]. Third, YY-23 selectively inhibited currents of GluN2C- and GluN2D-containing receptors (Fig. 1, D to G), unlike pore blockers such as ketamine, which display no subtype specificity (*42*). YY-23 predominantly inhibited the GluN2D-containing receptors in the hippocampus and cerebral cortex because the Glun2C is less expressed in these brain areas (fig. S5). The GluN2D subunit is specifically found in GABAergic interneurons of cerebral cortex (Fig. 3, A and B), conferring YY-23 with GABAergic selectivity. All these features may contribute to behavioral differences observed in rodents treated with YY-23 versus ketamine, where ketamine but not YY-23 induces dose-dependent hyperlocomotion and anesthetic effects (*43*, *44*).

In our in vitro studies, we observed that YY-23 inhibited NMDARs containing both GluN2C and GluN2D subunits. This finding raises a pertinent question regarding the potential role of the GluN2C subunit in mediating antidepressant effects. The GluN2C subunit is primarily located in the thalamus and cerebellum (*13*, *45*), and it is associated with motor and psychomimetic effects. Research conducted by Tarrés-Gatius *et al.* (*46*) reveals that while GluN2C KO mice did not exhibit the antidepressant and psychomimetic effects typically associated with ketamine, ketamine was still able to diminish psychomimetic behavior in these mice without affecting its antidepressant efficacy. The behavioral tests in the current research also showed that GluN2C did not involve in the antidepressant effect of YY-23 on mice. These findings suggest that the GluN2C-incorporated NMDARs may play a role in the psychomimetic effects induced by ketamine rather than its antidepressant effects. In contrast, our results suggest a more pronounced association of the GluN2D-incorporated NMDARs with antidepressant effects. This is exemplified by our observation that conditional knockout (cKO) of the GluN2D subunit in PV interneurons resulted in

an antidepressant-like phenotype (Fig. 6, D and E). These outcomes indicate a potential specificity of the GluN2D subunit in mediating antidepressant effects. However, it is imperative to acknowledge that further research is needed to conclusively determine the roles of these subunits in the complex mechanisms underlying antidepressant efficacy, especially when they assemble to triheteromeric NMDARs.

Preclinical and clinical studies have characterized the neuroanatomical and functional abnormalities of the PFC in MDD models and patients (*47*–*51*). The PFC is vulnerable to stress, and even brief and mild stressors can cause rapid dendritic shrinkage and marked prefrontal cognitive impairment (*52*, *53*). Aberrant gene expression and dysfunction of NMDARs in the PFC have been found in patients with MDD (*54*–*56*). A large number of studies have demonstrated that chronic stress gives rise to excitation/inhibition (E/I) imbalance in the PFC (*57*–*61*), which is strongly associated with depression. This has been further evidenced by the discovery that drugs targeting NMDARs can rectify the E/I imbalance. For example, ketamine has been proposed to act on NMDARs at GABAergic neurons (*62*), while the PAM rapastinel targets NMDARs at glutamatergic neurons (*15*). Although both drugs trigger different cell type–specific regulation of NMDARs, they ultimately exhibit promising antidepressant actions (*15*).

Consistent with the E/I balance theory, we found here that YY-23 precisely targeted GluN2D-containing subtype NMDARs at GABAergic interneurons. It reduced the inhibitory input (decreased APs and IPSCs) to pyramidal cells and indirectly enhanced excitatory transmission in the mPFC (Figs. 4 and *7* and fig. S6). On the basis of previous studies, NMDAR antagonists that induced pyramidal cell disinhibition may activate downstream signaling, including phospho-mTOR, brain-derived neurotrophic factor, and glutamatergic AMPARs mediated excitatory transmission, which will help reestablish synaptic communication that is impaired in depression (*63*, *64*). In this study, we confirmed that YY-23 increased excitatory synaptic transmission in the mPFC (fig. S6, I to Q). In addition, a 10-min application of YY-23 induced long-term potentiation (LTP) in hippocampal slices, as indicated by enhanced AMPAR-mediated fEPSPs (Fig. 8F) in the mPFC. This LTP effect was blocked by rapamycin, suggesting that mTOR signaling was involved in the synaptic plasticity mediated by YY-23. These findings demonstrated that GluN2D triggered pyramidal cell disinhibition, with the subsequent reestablishment of synaptic communication underlying the antidepressant effects of YY-23. Moreover, our study provided valuable insights for developing therapeutic antidepressant agents that target GluN2D-containing NMDARs.

MATERIALS AND METHODS

HPLC–tandem MS characterization of the synthetic YY-23

Timosaponin BIII was isolated from *Rhizoma Anemarrhenae*, which was purchased from the medicinal materials market of Shanghai (Shanghai City, China). High-performance liquid chromatography (HPLC)–grade acetonitrile was purchased from Dikma Company (Dikma, USA). The other reagents used were of analytical grade (Sinopharm Chemical Reagent Co. Ltd., China). Optical rotations were measured with a PerkinElmer 343 polarimeter. NMR spectra were measured on a Varian Mercury-400 (Varian, USA) using deuterium pyridine as the solvent and tetramethylsilane as an internal standard. HR-ESI-MS was carried out on a Micromass TOF Ultima (Micromass, UK) in negative electrospray (ESI−) ionization mode. Semipreparative HPLC was performed on a Unimicro Technologies System (quaternary pump, China) with a Grace Apollo C18 (10 mm inner diameter by 250 mm, octadecyl Silane, 5 μm) semipreparative HPLC column including an EasyGuard Kit C18 (4 mm by 2 mm) guard column; the detector was an ultraviolet detector.

Drug administration

For in vivo study, freshly prepared YY-23 was suspended in 1% carboxymethyl cellulose sodium. For acute administration, 1 hour before the behavioral tests, YY-23 was intragastrically administered, and midazolam or fluoxetine (Santa Cruz Biotechnology, USA) was intraperitoneally administered. All three drugs were chronically administered (once a day at 9:00 a.m. for 3 weeks) to control and susceptible mice. For in vitro study, YY-23 was first dissolved in DMSO and then diluted into extracellular recording solution for patch-clamp recording in HEK293T cells, Ringer solution for TEVC recording, or normal artificial cerebrospinal fluid (ACSF) for slice recording. Following a 7-day recovery period from surgery, rapamycin (10 nmol in 1 μl for PFC infusion) or a vehicle (DMSO) was administered at a rate of 0.25 μl/min using an injection cannula (26GA) that extended 0.5 mm beyond the guide cannula, 30 min before drug injections.

Plasmid construction

For electrophysiological study, pcDNA3.1-based expression plasmids encoding WT rat GluN1-1a (GenBank accession number U08261), GluN2A (GenBank accession number D13211), GluN2C (GenBank accession number M91563), GluN2D (GenBank accession number L31611), mouse GluN2B (GenBank accession number BC172745), human GluN2B (GenBank accession number U88963.1), and human GluN2D (NM_000836.4) were provided by P. Paoletti (Institut de Biologie de l'Ecole Normale Supérieure, France). We designed all the chimeric constructs based on segmenting of the GluN2 subunits. The S2-M4 linker segmented at Leu^{813}-Ile^{837} for human GluN2B and Ser^{825}-Lys^{839} for human GluN2D. In addition, the M4 segmented at Thr^{797}-Gln^{811} for human GluN2B and Leu^{840}-Ala^{864} for human GluN2D. All chimeric constructs were generated with a Gibson assembly kit (NEBuilder M5520AA). All the site-directed mutagenesis was introduced by PCR using primers that replaced homologous nucleic acid bases with mutant codons. pcDNA3.1-based expression plasmids encoding WT human nicotinic acetylcholine receptor alpha7 subunit (GenBank accession number U62436.1) was used. Complementary RNAs (cRNAs) of all these constructs were produced on the basis of restriction enzyme linearized cDNA templates using an RNA transcription kit (Invitrogen AM1345), and the quality was assessed by gel electrophoresis. For structural study, the cDNAs of WT *Homo sapiens grin1-1b* (Met^{1}-Gln^{868}, NM_001185090.2) and *grin2d* (Met^{1}-Pro^{879}, NM_000836.4) were cloned into pEG-BacMam vector (*65*).

TEVC recording

For TEVC recording, *X. laevis* oocytes were prepared, injected, and voltage-clamped as reported (*66*). Briefly, cRNAs or cDNAs of mixed GluN1-1a and GluN2 subunits at a 1:1 GluN1:GluN2 ratio or human Chrna7 were injected into oocytes followed by incubating at 15°C in Barth solution containing 88 mM NaCl, 10 mM Hepes, 1 mM KCl, 2.4 mM $NaHCO_3$, 0.33 mM $Ca(NO_3)_2$, 0.41 mM $CaCl_2$, and mM 0.82 $MgSO_4$ (pH adjusted to 7.6 with NaOH). For NMDARs, TEVC recordings were performed 24 to 48 hours after injection and conducted in Ringer solution containing 100 mM NaCl, 0.3 mM $BaCl_2$, 5 mM Hepes, and 0.01 mM diethylenetriamine pentaacetic acid

(pH adjusted to 7.3 with KOH with a final potassium concentration of approximately 2.5 mM). For α7 nicotinic acetylcholine receptor, TEVC recordings were performed 72 hours after injection and conducted in solution containing 115 mM NaCl, 2.5 mM KCl, 1.8 mM $CaCl_2$, and 10 mM Hepes (pH adjusted to 7.3 with NaOH). Both glass electrodes were filled with 3 M KCl solution, and the current responses were recorded using an OC-725 amplifier (Warner Instruments, Hamden, CT, USA) matched with a digital analog converter (Molecular Devices, Axon Digidata 1550B) under a holding potential of −60 mV unless performing the current-voltage ramp pulse. Glycine (100 μM) and glutamate (100 μM) were regarded as saturating agonists used to induce the current of NMDARs unless otherwise stated. We perfused YY-23 for 60 s, except for the GluN1-2A and GluN1-2B receptors, to adequately detect its effect. The DMSO used to dissolve the YY-23 was supplemented at the same concentration to each solution used in the same trace, but the total amount did not exceed 0.2%. All traces were analyzed with Clampfit 10.6 software, and individual traces were fitted using their own data points with Origin 8.0 for presentation. The current-voltage ramp pulses were recorded by clamping the oocytes successively at eight different voltages from −100 mV to +40 mV (20 mV apart) within 1 s for each voltage after perfusing the cells with YY-23 for 60 s without withdrawing the drug.

Patch-clamp recording of HEK293T cells

HEK293T cells (American Type Culture Collection, catalog no. CRL-3216) were maintained in Dulbecco's modified Eagle's medium/F12 (Gibco) supplemented with 10% fetal bovine serum (Gibco) and penicillin and penicillin-streptomycin (10 U ml^{-1}; Cellgro) in a humidified incubator at 37°C (5% CO_2). cDNAs encoding the NMDAR subunits and green fluorescent protein (GFP) at a ratio of 1:1:1 (GluN1:GluN2:GFP) were transiently transfected into HEK293T cells using Fugene HD transfection reagent (Invitrogen) and incubated for 12 to 16 hours. Whole-cell patch-clamp recordings were performed at −60 mV using Axopatch 700B (Molecular Devices). The amplification and data acquisition were performed using an Axon Digidata 1550B (Molecular Devices). The electrodes were filled with an internal solution containing the following 110 mM D-gluconate, 110 mM CsOH, 30 mM CsCl, 5 mM Hepes, 4 mM NaCl, 0.5 mM $CaCl_2$, 2 mM $MgCl_2$, 5 mM 1,2-bis(2-aminophenoxy)ethane-*N*,*N*,*N*′,*N*′-tetraacetic acid, 2 mM sodium ATP, and 0.3 mM sodium GTP (pH adjusted to 7.35 with CsOH). The extracellular recording solution was composed of the following 150 mM NaCl, 10 mM Hepes, 3 mM KCl, 0.5 mM $CaCl_2$, and 0.01 mM EDTA (pH adjusted to 7.4 with NaOH). We used 20 μM glycine and 500 μM NMDA to induce the current of NMDARs expressed on HEK293T cells. The current responses were filtered at 2 kHz (eight-pole Bessel filter, −3 dB) and digitized at 20 to 40 kHz.

Screening of pharmacological targets for YY-23 based on monoaminergic receptors

The FLIPR Calcium 4 Assay Kit (Molecular Devices) was used for the measurement of agonist- and antagonist-stimulated calcium signaling in cells (CHO-K1, Chempartner) expressing G protein–coupled receptors (GPCRs), including $5HT_{2A}$, $5HT_{2B}$, and $5HT_{2C}$. The activity levels of these GPCRs can be functionally assessed using FLIPR-based fluorescence assays (*67*, *68*). In addition, a Lance Ultra cAMP kit (Molecular Devices) was used to test the effects of compounds on $5HT_{1A}$, D_1R, D_2R, and D_4R in agonist and antagonist modes. The detail was described in Supplementary Materials and Methods.

Protein purification and cryo-EM sample preparation

Suspended HEK293S GnTI$^-$ cells at the concentration of 3.5 to 4.0×10^6/ml in 37°C were infected with P2 recombinant baculovirus encoding human *grin1b* and *grin2d*. A total of 10 μM MK-801 and 10 mM sodium butyrate were coadded into the culture medium for boosting protein expression. Cells were transferred to 30°C for additional 48 to 60 hours and then collected by centrifugation at 7000*g* for 20 min. To completely remove MK801 contamination, membrane fractions were extracted and further dialyzed in tris-buffered saline (TBS) buffer [150 mM NaCl and 20 mM tris (pH 8.0)] plus 1 mM glycine and 1 mM glutamate for 24 hours and TBS buffer for another 24 hours. Afterward, the membrane was solubilized in TBS containing 1% lauryl maltose neopentyl glycol (L-MNG), a protease inhibitor cocktail of 0.8 μM aprotinin, 2 mM pepstatin A, leupeptin (2 μg/ml), 1 mM phenylmethyl sulfonyl fluoride, 1 mM glycine, and 1 mM glutamate for 1.5 hours. After ultracentrifugation at 40,000 rpm, the supernatant was purified using Strep-tactin resin, and the protein was eluted with TBS buffer supplemented with 0.1% L-MNG and 5 mM D-desthiobiotin.

To incorporate the receptor in lipid nanodisc, soya bean lecithin (SBL; Avanti) dissolved in chloroform was dried down by nitrogen and resuspended in a TBS buffer supplemented with 20 mM L-MNG to a final lipid concentration of 10 mM. Recombinant expressed MSP1E3D1 protein (in *Escherichia coli*) was purified by metal chelate affinity column (Ni-nitrilotriaceate) and dialysis against TBS buffer. Then, a purified GluN1b-GluN2D receptor was mixed with MSP1E3D1 and SBL in a final ratio of 1:12:840 (molar ratios) and incubated for 40 min by gentle agitation at 4°C. Then, L-MNG was removed by adding Bio-Beads (SM2, Bio-Rad) to a final concentration of 150 mg/ml. After incubation for 2 hours, the Bio-Beads were replaced with fresh beads. The mixture was incubated overnight at 4°C. After separation from Bio-Beads, Superose 6 Increase column (GE Healthcare) was used for size exclusion chromatography in TBS buffer. Peak fractions corresponding to reconstituted NMDAR were collected and concentrated to approximately 2 mg/ml for cryo-EM sample preparation.

Glycine (1 mM), 600 μM *R*-CPP (Tocris, 0247-10), and 600 μM YY-23 were added into the protein sample and equilibrated by rotating for 30 min in 4°C. A three-microliter protein sample was applied to the glow-discharged 300-mesh Quantifoil R1.2/1.3 (Au) grid (Electron Microscopy China, BQR1.2/1.3-3A) using Vitrobot (Thermo Fisher Scientific), with the chamber environment controlled at 8°C and in 100% humidity. Grids were blotted for 3 s and immediately plunged into liquid ethane for vitrification.

Cryo-EM data acquisition and processing

Cryo-EM data were collected on 300-kV Titan Krios G3 electron microscope (FEI) equipped with a K3 Summit direct electron detector (Gatan) and a Gatan quantum energy filter. The pixel size in the super-resolution counting mode was set to 0.5355 Å, and each movie stack was dose-fractionated over 40 frames with a total dose of 60 electrons. The defocus values of movie stacks varied between −1.5 and −2.5 μm. Automatic data collection was conducted using Serial EM.

Data processing was mainly conducted by Relion 3.1.1 (*69*). Beam-induced motion and drift correction were performed using MotionCor2 (*70*). Contrast transfer function (CTF) parameters for each micrograph were determined by Gctf (*71*). Autopicked particles were extracted and then subjected to several rounds of reference-free two-dimensional (2D) classification and 3D classification. C2

symmetry was applied for the 3D refinement procedure. The "gold standard" fourier shell correlation (FSC) resolution was calculated with a soft shape mask applied to independent unfiltered half maps, with 0.143 criteria. Local resolution of density maps is estimated by using ResMap-1.1.461 (*72*).

Model building and refinement

Initial templates of N1b-N2D were generated with SWISS-MODEL (*73*), based on the structure of N1a-N2D receptor (PDB: 7YFF). Rigid-body docking with ChimeraX (*74*) was used to fit the structural coordinates into the density maps. The models were then subjected to iterative manual adjustment in Coot 0.9.6.1 (*75*) and real space refinement in Phenix 1.20.1 (*76*).

Animals

Adult male C57BL/6N mice aged 8 to 12 weeks were used for electrophysiological recording and behavioral tests. Adult male CD-1 mice aged 4 to 6 months were used as aggressors to develop a depressive model of CSDS. The mice were raised under stable conditions (except for the development of stressed mice) with access to food and water ad libitum. All animal studies and experimental procedures were approved by the Animal Care Committees of Shanghai Institute of Materia Medica (SYXK2020-0042) and the Center for Excellence in Brain Science and Intelligence Technology (NA-038-2023), Chinese Academy of Sciences. The experiments were carried out in accordance with European Union Directive 2010/63/EU on the protection of animals used for scientific purposes. Double-blind experiments with drug administration were conducted, and the animals were randomly divided into groups.

Transgenic mouse construction and validation

Grin2d$^{-/-}$ *and grin2d*$^{f/f}$ mice were generated with a CRISPR-Cas9 system at Biocytogen Pharmaceuticals (Beijing) Co. Ltd. according to Ikeda *et al.* (*77*). The deletion of exon 2 from the mouse genome terminates the protein translation in exon 3 via frameshift mutation and yielded the *Grin2d*$^{-/-}$ mice. Briefly, a pair of single guide RNAs (sgRNAs) (sgRNA 1: 5′ AGCCTGCGCCGCTCCGCATG 3′; sgRNA 13: 5′ TGGCAGAATGAGCCTAGTCT 3′) was designed to targeting the exon 2 segment of the *grin2d* gene (fig. S10A). For the *grin2d*$^{f/f}$ mice, a targeting vector that incorporated *loxP* fragments and exon 2 of *grin2d* was designed to insert into the cleavage gap between sgRNA 1 and sgRNA 13 sites (fig. S10B). The off-target effect validation of CRISPR-Cas9 system is shown in the Supplementary Materials (Supplementary Materials and Methods and fig. S10C). The *Grin2c* KO mouse was a gift from X. Cai (Oujiang Laboratory, Key Laboratory of Alzheimer's Disease of Zhejiang Province, Institute of Aging, School of Mental Health, Wenzhou Medical University, Wenzhou, Zhejiang 325035, China). Also, the PV-cre mouse (the Jackson Laboratory, stock no. 008069) was a gift from H. Yao (Institute of Neuroscience, State Key Laboratory of Neuroscience, Chinese Academy of Sciences Center for Excellence in Brain Science and Intelligence Technology, Chinese Academy of Sciences, Shanghai 200031, China). For cKO *grin2d* in PV^{+} neurons of mice, *grin2d*$^{f/f}$ mice were crossbred with a PV-cre mouse.

To further validate the gene expression of the *grin2d*-KO mice, we detected the mRNA expression level of *grin2d* by quantitative PCR. We extracted total RNA (kit no. B511311, Sangon Biotech) from the brain mPFC and hypothalamus tissues of WT and mutant mice and constructed a cDNA library using a cDNA reverse transcription kit (kit no. 18080044, Invitrogen). Then, we amplified *grin2d* (forward primer: 5′ GTGCTGGAGGAGTACGACTG 3′, reverse primer: 5′ GCAGAAGAAGTGGTTCCCCA 3′, used for amplifying a segment of *grin2d* exon 2) and a housekeeping gene, *gapdh* (as a control, forward primer: 5′ TGTGTCCGTCGTGGATCTGA 3′, reverse primer: 5′ TTGCTGTTGAAGTCGCAGGAG 3′), and analyzed all the PCR products by agarose gel electrophoresis (Fig. 3J).

Multiplex FISH

Mice were perfused intracardially with diethyl pyrocarbonate (DEPC)–phosphate-buffered saline (PBS) followed by ice-cold 4% paraformaldehyde (PFA) in PBS. The brains were dissected, postfixed in 4% PFA for 12 to 24 hours at 4°C, and dehydrated with 30% sucrose in DEPC-PBS. Afterward, the brains were sectioned at 20-μm thickness and mounted on SuperFrost Plus Slides (Thermo Fisher Scientific). Multiplex FISH was then performed with an RNAscope Multiplex Fluorescent v2-Kit (ACDBio). Probes against *grin2d* mRNA, *Slc32a1* mRNA, and *Slc17a7* mRNA were ordered from ACDBio and used in the experiment. Images were captured under a ×20 or ×63 objective using a confocal microscope (Lecia TCS SP5 CFSMP).

Slice preparation

Mice were anesthetized with isoflurane, euthanized, and then perfused with 20 ml of ice-cold, oxygenated ACSF (25.0 mM $NaHCO_3$, 1.25 mM NaH_2PO_4, 2.5 mM KCl, 0.5 $CaCl_2$, 7.0 mM $MgCl_2$, 25.0 mM glucose, 11.0 mM choline chloride, 11.6 mM ascorbic acid, and 3.1 mM pyruvic acid, gassed with 95% O_2 and 5% CO_2). The brains were immediately dissected out after decapitation. Bilateral coronal slices containing the medial PFC (350-μm thick) were cut using a vibratome (Leica VT1000s, USA). The slices were quickly placed into a chamber and incubated in normal oxygenated ACSF (118 mM NaCl, 2.5 mM KCl, 26 mM $NaHCO_3$, 1 mM NaH_2PO_4, 10 mM glucose, 1.3 mM $MgCl_2$, and 2.5 mM $CaCl_2$, gassed with 95% O_2 and 5% CO_2) at 35°C for 2 hours. The slices were lastly transferred to the recording chamber at room temperature.

Electrophysiology in mPFC slices

Electrophysiological recordings of features including APs, sIPSCs, mIPSCs, fEPSPs, and mEPSCs were carried out using an experimental device composed of an Axopatch 700B amplifier (Molecular Devices) and an Olympus microscope (Olympus, Japan) equipped with infrared differential interference contrast optics. The expression of EGFP was visualized in interneurons in the acute slice preparation of GAD67-EGFP knock-in mice using epifluorescence illumination. The APs of interneurons in layer II/III and the mEPSCs of pyramidal neurons in layer V in the prelimbic mPFC were recorded by the whole-cell patch-clamp technique. The glass electrodes had a resistance tip in the range of 3 to 4 megohm. For AP recording, the pipettes were filled with intracellular solution containing 114 mM potassium gluconate, 6 mM KCl, 0.5 mM $CaCl_2$, 0.2 mM EGTA, 4 mM ATP-Mg, and 10 Hepes (pH adjusted to 7.25 with NaOH). AP firing was evoked in current-clamp mode by current injection. For the IPSC recording, the internal solution contains the following: 130 mM Cs-methanesulfonate, 10 mM CsCl, 10 mM Hepes, 4 mM NaCl, 7 mM phosphocreatine, 0.3 mM Na-GTP, 4 mM Mg-ATP, and 2 mM QX314-Br (pH adjusted to ~7.3 with CsOH). sIPSCs were recorded in the mPFC pyramidal neurons voltage clamped at +10 mV, and mIPSCs were recorded in the presence of tetrodotoxin (TTX). For the mEPSC recording, neurons were clamped at −65 mV in the presence of TTX (1 μM) and bicuculline

(10 μM) in ACSF solution. The intracellular solution contained 115 mM $CsMeSO_3$, 20 mM CsCl, 10 mM Hepes, 2.5 mM $MgCl_2$, 4 mM Na2-ATP, 0.4 mM Na-GTP, 10 mM Na-phosphocreatine, and 0.6 mM EGTA (pH adjusted to 7.0 with NaOH). The data were filtered at 1 kHz and sampled at 10 kHz using Axon Digidata 1550B (Molecular Devices, USA) and analyzed by the Mini Analysis Program (Synaptosoft). For fEPSP recording, the bipolar stimulating electrode was placed on layer V of the mPFC slice, and the recording electrode (filled with 0.5 M CH_3COONa, 1- to 5-megohm resistance at the tip) was placed on layer II/III. The duration of the stimulus pulse was 100 μs with delivery at 0.03 Hz, and the stimulus intensity was adjusted to 65% of the maximal response. When the evoked responses were maintained at a stable level at this intensity, additional baseline recording was performed for 10 min before the drug treatment. All recordings were continued for 60 to 80 min. NMDA-evoked currents were recorded in the presence of 200 μM NMDA and 30 μM glycine, which were pressurized and applied in a brief pulse. After 3 to 5 stable NMDA-evoked currents in the ACSF solution, 3 μM CIQ, 20 μM YY-23, or both were bath-applied for 15 to 20 min. Current responses were then evoked again by pressure application of NMDA and glycine and compared with current responses obtained during application of the control (ACSF).

Novelty-suppressed feeding test in mice

Mice were deprived of food for 24 hours with access to water ad libitum before the test was carried out. The mice were then removed to the test room and placed into a clean cage to habituate for at least 1 hour. The testing apparatus consisted of a Plexiglas box (40 cmby 40 cm by 20 cm), the floor of which was covered with 2 cm of wooden bedding. A small piece of mouse chow was placed on a white platform (white circular filter paper, 11 cm in diameter) positioned in the center of the box. Each mouse was then placed in a corner of the box with his head facing the platform. The latency of first feeding episode was recorded. The first successful feeding was defined by the mouse sitting on its haunches, holding the pellet with its forepaws and biting the pellets. Immediately after the first feeding, each mouse was transferred to his home cage with access to food ad libitum, and the amount of food consumed was measured to control for a change in appetite as a possible confounding factor.

Force swimming test

This test was conducted under normal light, as previously described (*78*). Briefly, mice were individually placed in a cylinder (35 cm in height × 10 cm in diameter) filled with water. An appropriate water level was set to prevent each mouse from touching the bottom with its limbs. In addition, the water temperature was set at 23° to 25°C. The mice were allowed to swim for 6 min, and their activity was videotaped. There had been an extra acclimation period with a 10-min swim on the previous day. The duration of immobility, defined as the time spent floating or remaining motionless, was quantified manually during the last 4 min.

Open field test

The OFT is a standard method to profile locomotor activity. Briefly, mice were handled in advance and then placed into the center of a square box (100 cm by 100 cm by 45 cm) that was made of white acrylic plastic. Each mouse was allowed to explore in the box for 10 min and was monitored online. The distance moved and percent of distance traveled in the center area for each animal were calculated offline.

Tail suspension test

The mice were suspended by securing their tails on the edge of a shelf positioned at a height of 80 cm above the floor. Their activity was videotaped to analyze their escape behavior. A blinded experiment was conducted to record the amount of time spent immobile during the last 4 min of the testing period; the first 2 min was excluded.

Procedure for the development of a mouse depressive model of CSDS

As previously described (*27*), briefly, after screening to identify aggressive CD-1 mice, intruder C57BL/6N mice were directly placed within the resident aggressor's home cage compartment for 5 to 10 min on 10 consecutive days. During this exposure, the intruders showed signs of stress and subordination, including vocalization, the flight response, and a submissive posture. To prevent any habituation to the resident aggressor, the intruder C57BL/6J was exposed to a new resident's home cage compartment for each subsequent daily defeat. After 5 to 10 min of social defeat, the intruder was transported across the perforated divider to the opposite compartment and house in this compartment for the remainder of the 24-hour period.

We placed the control C57BL/6N mice that did not experience social defeat in the same compartment. Twenty-four hours after the last session, we screened the susceptible mice based on the SI ratio. Briefly, SI was obtained by dividing the time spent in the interaction zone when the target was present by the time spent in the interaction zone when the target was absent. An SI ratio of less than 1 indicates that less time was spent in the presence than in the absence of a social aggressor. This can be used as a threshold for identifying susceptible mice. All mice were then housed individually for 3 weeks, and all of the susceptible mice were randomly divided into three groups for drug administration. The time spent in the interaction zone was accessed weekly using the same method as previously described (*27*).

Corticosterone-induced depression

Corticosterone (35 μg ml^{-1}, Sigma-Aldrich), dissolved in 0.45% 2-hydroxypropyl-β-cyclodextrin (0.45% HP-β-CD) or vehicle (0.45% HP-β-CD), was added to the drinking water and made available ad libitum. C57BL/6J mice were provided with the corticosterone (CORT) solution for 2 weeks and gradually weaned off over another 6 days by halving the doses every other day. To prevent degradation, the CORT solution was replaced every 2 days.

Proteogenomic analysis by MS

Twenty-four hours after the last session of behavioral tests with the mouse depressive model of CSDS, the brain tissue of PFC regions was drowned immediately. Also, the protein of the tissue was further processed by tryptic digestion for subsequent MS analysis. The proteogenomic analysis of the PFC samples was performed on a Q-Exactive mass spectrometer with an ancillary EASY-nLC 1000 HPLC system (Thermo Fisher Scientific). The protein concentration was determined by tryptophan fluorescence emission assay as described previously (*79*) Afterward, approximately 100 μg of protein from each sample was processed by filter-aided sample preparation digestion as previously described (*80*). The raw proteomic data have been deposited to the ProteomeXchange (*81*) Consortium via the PRoteomics IDEntifications Database (PRIDE) (*82*) partner repository with the dataset identifier. All the detail was described in Supplementary Materials and Methods.

Data analysis

We calculated the relative current after YY-23 application to evaluate the effects of YY-23 on all WT, truncated, and other mutant NMDARs expressed in recombinant systems. We used IC_{50}, the concentration that inhibits the response half-maximally, to evaluate the YY-23 efficiency. The IC_{50} values were determined by nonlinear least-squares fitting of a Hill equation

$$Y = A + \frac{1 - A}{1 + 10^{(\mathrm{LogIC}_{50} - [X])^{n_H}}}$$

with concentration-response data from individual trials normalized to the maximal responses in the absence of inhibitor. In this equation, A is the minimal plateau of the dose-response curve; the relative current (Y) was measured at the 60th second of YY-23 application on oocytes and at the current plateaus for HEK293T cells; X is the YY-23 concentration; and n_H is the Hill slope. Fitted IC_{50} and Hill slope values for individual oocytes were used to calculate the mean and SEM as the final IC_{50} and Hill slope values. For voltage-current data analysis, we present the mean values with their associated SEM error bars.

To screen the pharmacological targets for YY-23 among monoaminergic receptors, calcium flux was measured by the FLIPR signal (FLIPR Calcium 4 Assay Kit), and cyclic adenosine 3′,5′-monophosphate (cAMP) was measured by the time-resolved fluorescence resonance energy transfer (TR-FRET) signal (Lance Ultra cAMP kit). The data are reported as the mean from the experiment. Median effective concentration (EC_{50}) [log(agonist) versus response − variable slope]: Y = bottom + (top-bottom)/(1 + 10^[(logEC_{50} − X) × hill slope]. IC_{50} [log(inhibitor) versus response − variable slope]: Y = bottom + (top-bottom)/(1 + 10^[(logIC_{50} − X) × hill slope]. GraphPad Prism software was used for data analysis and EC_{50} or IC_{50} calculation: Activation % $= \frac{\text{raw data} - \text{minimum signal}}{\text{maximum signal} - \text{minimum signal}} \times 100$ and inhibition % $= 100 - \frac{\text{raw data} - \text{minimum signal}}{\text{maximum signal} - \text{minimum signal}} \times 100$ for the targets $5HT_{1A}$, D_2R, D_4R, $5HT_{2A}$, $5HT_{2B}$, and $5HT_{2C}$; activation% $= 100 - \frac{\text{raw data} - \text{minimum signal}}{\text{maximum signal} - \text{minimum signal}} \times 100$ and inhibition % $= \frac{\text{raw data} - \text{minimum signal}}{\text{maximum signal} - \text{minimum signal}} \times 100$ for the target D_1R. The data analysis of MS was described in Supplementary Materials and Methods.

Statistical analyses

Data meeting the assumptions of normality and equal variance between sample groups are shown as the mean ± SEM. Data that did not meet the normality or equal variance assumptions are presented in box plots with bars showing the medians and boxes showing the lower/upper quartiles. All statistical tests were two-tailed, and significance was assigned at $P < 0.05$. The analyses were blindly performed for treatment assignments in all behavioral experiments. The statistical analyses were performed using GraphPad Prism v6 software. Normality and homogeneity of variance between group samples were assessed using the Shapiro-Wilk test and Bartlett's test, respectively. Once normality and equal variance between sample groups were achieved, *t* tests, one-way, and two-way analysis of variance (ANOVA) followed by post hoc multiple comparisons tests were used. When normality tests failed, Mann-Whitney *U*, Wilcoxon, Kruskal-Wallis one-way ANOVA, and Friedman's two-way ANOVA tests were performed. When homogeneity of variance tests failed, unpaired *t* test with Welch's correction and Brown-Forsythe ANOVA was used. In rare cases in which values were missing randomly from repeated-measures samples, the data were analyzed by fitting a mixed-effect model in Prism 9. The sample sizes, specific statistical tests used, and main effects of statistical analyses for each experiment are reported in the figure legends.

Supplementary Materials

This PDF file includes:

Supplementary Materials and Methods
Figs. S1 to S10
Tables S1 to S4

REFERENCES AND NOTES

1. G. S. Malhi, J. J. Mann, Depression. *Lancet* **392**, 2299–2312 (2018).
2. B. N. Gaynes, D. Warden, M. H. Trivedi, S. R. Wisniewski, M. Fava, A. J. Rush, What did STAR*D teach us? Results from a large-scale, practical, clinical trial for patients with depression. *Psychiatr. Serv.* **60**, 1439–1445 (2009).
3. B. Kadriu, L. Musazzi, I. D. Henter, M. Graves, M. Popoli, C. A. Zarate Jr., Glutamatergic neurotransmission: Pathway to developing novel rapid-acting antidepressant treatments. *Int. J. Neuropsychopharmacol.* **22**, 119–135 (2019).
4. C. Tomasetti, C. Montemitro, A. L. C. Fiengo, C. Santone, L. Orsolini, A. Valchera, A. Carano, M. Pompili, G. Serafini, G. Perna, F. Vellante, G. Martinotti, M. D. Giannantonio, Y. K. Kim, M. D. Nicola, A. Bellomo, A. Ventriglio, M. Fornaro, D. D. Berardis, Novel pathways in the treatment of major depression: Focus on the glutamatergic system. *Curr. Pharm. Des.* **25**, 381–387 (2019).
5. R. M. Berman, A. Cappiello, A. Anand, D. A. Oren, G. R. Heninger, D. S. Charney, J. H. Krystal, Antidepressant effects of ketamine in depressed patients. *Biol. Psychiatry* **47**, 351–354 (2000).
6. N. Li, B. Lee, R. J. Liu, M. Banasr, J. M. Dwyer, M. Iwata, X. Y. Li, G. Aghajanian, R. S. Duman, mTOR-dependent synapse formation underlies the rapid antidepressant effects of NMDA antagonists. *Science* **329**, 959–964 (2010).
7. A. E. Autry, M. Adachi, E. Nosyreva, E. S. Na, M. F. Los, P. F. Cheng, E. T. Kavalali, L. M. Monteggia, NMDA receptor blockade at rest triggers rapid behavioural antidepressant responses. *Nature* **475**, 91–95 (2011).
8. Y. Zhang, F. Ye, T. Zhang, S. Lv, L. Zhou, D. Du, H. Lin, F. Guo, C. Luo, S. Zhu, Structural basis of ketamine action on human NMDA receptors. *Nature* **596**, 301–305 (2021).
9. H. Homayoun, B. Moghaddam, NMDA receptor hypofunction produces opposite effects on prefrontal cortex interneurons and pyramidal neurons. *J. Neurosci.* **27**, 11496–11500 (2007).
10. J. M. Stone, C. Dietrich, R. Edden, M. A. Mehta, S. De Simoni, L. J. Reed, J. H. Krystal, D. Nutt, G. J. Barker, Ketamine effects on brain GABA and glutamate levels with 1H-MRS: Relationship to ketamine-induced psychopathology. *Mol. Psychiatry* **17**, 664–665 (2012).
11. R. N. Moda-Sava, M. H. Murdock, P. K. Parekh, R. N. Fetcho, B. S. Huang, T. N. Huynh, J. Witztum, D. C. Shaver, D. L. Rosenthal, E. J. Alway, K. Lopez, Y. Meng, L. Nellissen, L. Grosenick, T. A. Milner, K. Deisseroth, H. Bito, H. Kasai, C. Liston, Sustained rescue of prefrontal circuit dysfunction by antidepressant-induced spine formation. *Science* **364**, eaat8078 (2019).
12. P. Paoletti, C. Bellone, Q. Zhou, NMDA receptor subunit diversity: Impact on receptor properties, synaptic plasticity and disease. *Nat. Rev. Neurosci.* **14**, 383–400 (2013).
13. H. Monyer, N. Burnashev, D. J. Laurie, B. Sakmann, P. H. Seeburg, Developmental and regional expression in the rat brain and functional properties of four NMDA receptors. *Neuron* **12**, 529–540 (1994).
14. K. B. Hansen, L. P. Wollmuth, D. Bowie, H. Furukawa, F. S. Menniti, A. I. Sobolevsky, G. T. Swanson, S. A. Swanger, I. H. Greger, T. Nakagawa, C. J. McBain, V. Jayaraman, C. M. Low, M. L. Dell'Acqua, J. S. Diamond, C. R. Camp, R. E. Perszyk, H. Yuan, S. F. Traynelis, Structure, function, and pharmacology of glutamate receptor ion channels. *Pharmacol. Rev.* **73**, 298–487 (2021).
15. S. Pothula, T. Kato, R. J. Liu, M. Wu, D. Gerhard, R. Shinohara, A. N. Sliby, G. M. I. Chowdhury, K. L. Behar, G. Sanacora, P. Banerjee, R. S. Duman, Cell-type specific modulation of NMDA receptors triggers antidepressant actions. *Mol. Psychiatry* **26**, 5097–5111 (2021).
16. D. Y. Gawande, K. K. S. Narasimhan, G. P. Shelkar, R. Pavuluri, H. A. F. Stessman, S. M. Dravid, GluN2D subunit in parvalbumin interneurons regulates prefrontal cortex feedforward inhibitory circuit and molecular networks relevant to schizophrenia. *Biol. Psychiatry* **94**, 297–309 (2023).
17. K. Nakazawa, V. Jeevakumar, K. Nakao, Spatial and temporal boundaries of NMDA receptor hypofunction leading to schizophrenia. *NPJ Schizophr.* **3**, 7 (2017).
18. S. E. Kotermanski, J. W. Johnson, Mg^{2+} imparts NMDA receptor subtype selectivity to the Alzheimer's drug memantine. *J. Neurosci.* **29**, 2774–2779 (2009).

19. S. Ide, Y. Ikekubo, M. Mishina, K. Hashimoto, K. Ikeda, Role of NMDA receptor GluN2D subunit in the antidepressant effects of enantiomers of ketamine. *J. Pharmacol. Sci.* **135**, 138–140 (2017).
20. F. Guo, Q. Zhang, B. Zhang, Z. Fu, B. Wu, C. Huang, Y. Li, Burst-firing patterns in the prefrontal cortex underlying the neuronal mechanisms of depression probed by antidepressants. *Eur. J. Neurosci.* **40**, 3538–3547 (2014).
21. Q. Zhang, F. Guo, Z. W. Fu, B. Zhang, C. G. Huang, Y. Li, Timosaponin derivative YY-23 acts as a non-competitive NMDA receptor antagonist and exerts a rapid antidepressant-like effect in mice. *Acta Pharmacol. Sin.* **37**, 166–176 (2016).
22. Z. Liu, W. Jiang, B. Wu, C. Huang, New saponins from timosaponin BIII by acid hydrolysis. *Asian J. Chem.* **25**, 2503–2505 (2013).
23. J. Zhang, M. Zhang, Q. Wang, H. Wen, Z. Liu, F. Wang, Y. Wang, F. Yao, N. Song, Z. Kou, Y. Li, F. Guo, S. Zhu, Distinct structure and gating mechanism in diverse NMDA receptors with GluN2C and GluN2D subunits. *Nat. Struct. Mol. Biol.* **30**, 629–639 (2023).
24. P. Paoletti, Molecular basis of NMDA receptor functional diversity. *Eur. J. Neurosci.* **33**, 1351–1365 (2011).
25. G. J. Salimando, M. Hyun, K. M. Boyt, D. G. Winder, BNST GluN2D-containing NMDA receptors influence anxiety- and depressive-like behaviors and modulate cell-specific excitatory/inhibitory synaptic balance. *J. Neurosci.* **40**, 3949–3968 (2020).
26. P. Mullasseril, K. B. Hansen, K. M. Vance, K. K. Ogden, H. Yuan, N. L. Kurtkaya, R. Santangelo, A. G. Orr, P. Le, K. M. Vellano, D. C. Liotta, S. F. Traynelis, A subunit-selective potentiator of NR2C- and NR2D-containing NMDA receptors. *Nat. Commun.* **1**, 90 (2010).
27. S. A. Golden, H. E. Covington III, O. Berton, S. J. Russo, A standardized protocol for repeated social defeat stress in mice. *Nat. Protoc.* **6**, 1183–1191 (2011).
28. C. A. Hoeffer, E. Klann, mTOR signaling: At the crossroads of plasticity, memory and disease. *Trends Neurosci.* **33**, 67–75 (2010).
29. A. J. Eisch, D. Petrik, Depression and hippocampal neurogenesis: A road to remission? *Science* **338**, 72–75 (2012).
30. S. F. Traynelis, L. P. Wollmuth, C. J. McBain, F. S. Menniti, K. M. Vance, K. K. Ogden, K. B. Hansen, H. Yuan, S. J. Myers, R. Dingledine, Glutamate receptor ion channels: Structure, regulation, and function. *Pharmacol. Rev.* **62**, 405–496 (2010).
31. S. F. Traynelis, M. Hartley, S. F. Heinemann, Control of proton sensitivity of the NMDA receptor by RNA splicing and polyamines. *Science* **268**, 873–876 (1995).
32. M. Horak, K. Vlcek, H. Chodounska, L. Vyklicky Jr., Subtype-dependence of N-methyl-D-aspartate receptor modulation by pregnenolone sulfate. *Neuroscience* **137**, 93–102 (2006).
33. C. A. Mosley, T. M. Acker, K. B. Hansen, P. Mullasseril, K. T. Andersen, P. Le, K. M. Vellano, H. Brauner-Osborne, D. C. Liotta, S. F. Traynelis, Quinazolin-4-one derivatives: A novel class of noncompetitive NR2C/D subunit-selective N-methyl-D-aspartate receptor antagonists. *J. Med. Chem.* **53**, 5476–5490 (2010).
34. T. M. Acker, H. Yuan, K. B. Hansen, K. M. Vance, K. K. Ogden, H. S. Jensen, P. B. Burger, P. Mullasseril, J. P. Snyder, D. C. Liotta, S. F. Traynelis, Mechanism for noncompetitive inhibition by novel GluN2C/D N-methyl-D-aspartate receptor subunit-selective modulators. *Mol. Pharmacol.* **80**, 782–795 (2011).
35. J. Monod, J. Wyman, J. P. Changeux, On the nature of allosteric transitions: A plausible model. *J. Mol. Biol.* **12**, 88–118 (1965).
36. D. Bertrand, M. Gopalakrishnan, Allosteric modulation of nicotinic acetylcholine receptors. *Biochem. Pharmacol.* **74**, 1155–1163 (2007).
37. S. Zhu, P. Paoletti, Allosteric modulators of NMDA receptors: Multiple sites and mechanisms. *Curr. Opin. Pharmacol.* **20**, 14–23 (2015).
38. P. Banerjee, J. E. Donello, B. Hare, R. S. Duman, Rapastinel, an NMDAR positive modulator, produces distinct behavioral, sleep, and EEG profiles compared with ketamine. *Behav. Brain Res.* **391**, 112706 (2020).
39. T. H. Chou, M. Epstein, K. Michalski, E. Fine, P. C. Biggin, H. Furukawa, Structural insights into binding of therapeutic channel blockers in NMDA receptors. *Nat. Struct. Mol. Biol.* **29**, 507–518 (2022).
40. J. F. Macdonald, Z. Miljkovic, P. Pennefather, Use-dependent block of excitatory amino-acid currents in cultured neurons by ketamine. *J. Neurophysiol.* **58**, 251–266 (1987).
41. C. R. Honey, Z. Miljkovic, J. F. Macdonald, Ketamine and phencyclidine cause a voltage-dependent block of responses to L-aspartic acid. *Neurosci. Lett.* **61**, 135–139 (1985).
42. T. Yamakura, K. Sakimura, K. Shimoji, The stereoselective effects of ketamine isomers on heteromeric-methyl-D-aspartate receptor channels. *Anesth. Analg.* **91**, 225–229 (2000).
43. P. Zanos, T. D. Gould, Mechanisms of ketamine action as an antidepressant. *Mol. Psychiatry* **23**, 801–811 (2018).
44. T. Hayase, Y. Yamamoto, K. Yamamoto, Behavioral effects of ketamine and toxic interactions with psychostimulants. *BMC Neurosci.* **7**, 25 (2006).
45. Y. Suzuki, C. Nakamoto, I. Watanabe-Iida, M. Watanabe, T. Takeuchi, T. Sasaoka, M. Abe, K. Sakimura, Quantitative analysis of NMDA receptor subunits proteins in mouse brain. *Neurochem. Int.* **165**, 105517 (2023).
46. M. Tarrés-Gatius, L. Miquel-Rio, L. Campa, F. Artigas, A. Castane, Involvement of NMDA receptors containing the GluN2C subunit in the psychotomimetic and antidepressant-like effects of ketamine. *Transl. Psychiatry* **10**, 427 (2020).
47. W. Coryell, P. Nopoulos, W. Drevets, T. Wilson, N. C. Andreasen, Subgenual prefrontal cortex volumes in major depressive disorder and schizophrenia: Diagnostic specificity and prognostic implications. *Am. J. Psychiatry* **162**, 1706–1712 (2005).
48. B. W. Dunlop, J. K. Rajendra, W. E. Craighead, M. E. Kelley, C. L. McGrath, K. S. Choi, B. Kinkead, C. B. Nemeroff, H. S. Mayberg, Functional connectivity of the subcallosal cingulate cortex and differential outcomes to treatment with cognitive-behavioral therapy or antidepressant medication for major depressive disorder. *Am. J. Psychiatry* **174**, 533–545 (2017).
49. T. Wise, J. Radua, E. Via, N. Cardoner, O. Abe, T. M. Adams, F. Amico, Y. Cheng, J. H. Cole, C. de Azevedo Marques Perico, D. P. Dickstein, T. F. D. Farrow, T. Frodl, G. Wagner, I. H. Gotlib, O. Gruber, B. J. Ham, D. E. Job, M. J. Kempton, M. J. Kim, P. Koolschijn, G. S. Malhi, D. Mataix-Cols, A. M. McIntosh, A. C. Nugent, J. T. O'Brien, S. Pezzoli, M. L. Phillips, P. S. Sachdev, G. Salvadore, S. Selvaraj, A. C. Stanfield, A. J. Thomas, M. J. van Tol, N. J. A. van der Wee, D. J. Veltman, A. H. Young, C. H. Fu, A. J. Cleare, D. Arnone, Common and distinct patterns of grey-matter volume alteration in major depression and bipolar disorder: Evidence from voxel-based meta-analysis. *Mol. Psychiatry* **22**, 1455–1463 (2017).
50. E. L. Belleau, M. T. Treadway, D. A. Pizzagalli, The impact of stress and major depressive disorder on hippocampal and medial prefrontal cortex morphology. *Biol. Psychiatry* **85**, 443–453 (2019).
51. Y. Luo, Q. Xiao, J. Wang, L. Jiang, M. Hu, Y. Jiang, J. Tang, X. Liang, Y. Qi, X. Dou, Y. Zhang, C. Huang, L. Chen, Y. Tang, Running exercise protects oligodendrocytes in the medial prefrontal cortex in chronic unpredictable stress rat model. *Transl. Psychiatry* **9**, 322 (2019).
52. A. Izquierdo, C. L. Wellman, A. Holmes, Brief uncontrollable stress causes dendritic retraction in infralimbic cortex and resistance to fear extinction in mice. *J. Neurosci.* **26**, 5733–5738 (2006).
53. A. F. T. Arnsten, Stress signalling pathways that impair prefrontal cortex structure and function. *Nat. Rev. Neurosci.* **10**, 410–422 (2009).
54. O. Kaut, I. Schmitt, A. Hofmann, P. Hoffmann, T. E. Schlaepfer, U. Wullner, R. Hurlemann, Aberrant NMDA receptor DNA methylation detected by epigenome-wide analysis of hippocampus and prefrontal cortex in major depression. *Eur. Arch. Psychiatry Clin. Neurosci.* **265**, 331–341 (2015).
55. W. N. Marsden, Stressor-induced NMDAR dysfunction as a unifying hypothesis for the aetiology, pathogenesis and comorbidity of clinical depression. *Med. Hypotheses* **77**, 508–528 (2011).
56. M. D. Underwood, M. J. Bakalian, V. L. Johnson, S. A. Kassir, S. P. Ellis, J. J. Mann, V. Arango, Less NMDA receptor binding in dorsolateral prefrontal cortex and anterior cingulate cortex associated with reported early-life adversity but not suicide. *Int. J. Neuropsychopharmacol.* **23**, 311–318 (2020).
57. M. Popoli, Z. Yan, B. S. McEwen, G. Sanacora, The stressed synapse: The impact of stress and glucocorticoids on glutamate transmission. *Nat. Rev. Neurosci.* **13**, 22–37 (2011).
58. E. Y. Yuen, J. Wei, W. Liu, P. Zhong, X. Li, Z. Yan, Repeated stress causes cognitive impairment by suppressing glutamate receptor expression and function in prefrontal cortex. *Neuron* **73**, 962–977 (2012).
59. J. M. McKlveen, R. L. Morano, M. Fitzgerald, S. Zoubovsky, S. N. Cassella, J. R. Scheimann, S. Ghosal, P. Mahbod, B. A. Packard, B. Myers, M. L. Baccei, J. P. Herman, Chronic stress increases prefrontal inhibition: A mechanism for stress-induced prefrontal dysfunction. *Biol. Psychiatry* **80**, 754–764 (2016).
60. M. S. Lener, M. J. Niciu, E. D. Ballard, M. Park, L. T. Park, A. C. Nugent, C. A. Zarate Jr., Glutamate and gamma-aminobutyric acid systems in the pathophysiology of major depression and antidepressant response to ketamine. *Biol. Psychiatry* **81**, 886–897 (2017).
61. C. E. Page, L. Coutellier, Prefrontal excitatory/inhibitory balance in stress and emotional disorders: Evidence for over-inhibition. *Neurosci. Biobehav. Rev.* **105**, 39–51 (2019).
62. D. M. Gerhard, S. Pothula, R. J. Liu, M. Wu, X. Y. Li, M. J. Girgenti, S. R. Taylor, C. H. Duman, E. Delpire, M. Picciotto, E. S. Wohleb, R. S. Duman, GABA interneurons are the cellular trigger for ketamine's rapid antidepressant actions. *J. Clin. Invest.* **130**, 1336–1349 (2020).
63. R. S. Duman, G. K. Aghajanian, Synaptic dysfunction in depression: Potential therapeutic targets. *Science* **338**, 68–72 (2012).
64. R. S. Duman, G. K. Aghajanian, G. Sanacora, J. H. Krystal, Synaptic plasticity and depression: New insights from stress and rapid-acting antidepressants. *Nat. Med.* **22**, 238–249 (2016).
65. A. Goehring, C. H. Lee, K. H. Wang, J. C. Michel, D. P. Claxton, I. Baconguis, T. Althoff, S. Fischer, K. C. Garcia, E. Gouaux, Screening and large-scale expression of membrane proteins in mammalian cells for structural studies. *Nat. Protoc.* **9**, 2574–2585 (2014).
66. M. Gielen, A. Le Goff, D. Stroebel, J. W. Johnson, J. Neyton, P. Paoletti, Structural rearrangements of NR1/NR2A NMDA receptors during allosteric inhibition. *Neuron* **57**, 80–93 (2008).
67. Q. Ma, L. Ye, H. Liu, Y. Shi, N. Zhou, An overview of Ca^{2+} mobilization assays in GPCR drug discovery. *Expert Opin. Drug Discovery* **12**, 511–523 (2017).
68. G. Woszczek, E. Fuerst, Ca^{2+} mobilization assays in GPCR drug discovery. *Methods Mol. Biol.* **1272**, 79–89 (2015).
69. S. H. Scheres, RELION: Implementation of a Bayesian approach to cryo-EM structure determination. *J. Struct. Biol.* **180**, 519–530 (2012).

70. S. Q. Zheng, E. Palovcak, J. P. Armache, K. A. Verba, Y. Cheng, D. A. Agard, MotionCor2: Anisotropic correction of beam-induced motion for improved cryo-electron microscopy. *Nat. Methods* **14**, 331–332 (2017).
71. K. Zhang, Gctf: Real-time CTF determination and correction. *J. Struct. Biol.* **193**, 1–12 (2016).
72. A. Kucukelbir, F. J. Sigworth, H. D. Tagare, Quantifying the local resolution of cryo-EM density maps. *Nat. Methods* **11**, 63–65 (2014).
73. K. Arnold, L. Bordoli, J. Kopp, T. Schwede, The SWISS-MODEL workspace: A web-based environment for protein structure homology modelling. *Bioinformatics* **22**, 195–201 (2006).
74. E. F. Pettersen, T. D. Goddard, C. C. Huang, E. C. Meng, G. S. Couch, T. I. Croll, J. H. Morris, T. E. Ferrin, UCSF ChimeraX: Structure visualization for researchers, educators, and developers. *Protein Sci.* **30**, 70–82 (2021).
75. P. Emsley, K. Cowtan, Coot: Model-building tools for molecular graphics. *Acta Crystallogr. D Biol. Crystallogr.* **60**, 2126–2132 (2004).
76. P. V. Afonine, B. K. Poon, R. J. Read, O. V. Sobolev, T. C. Terwilliger, A. Urzhumtsev, P. D. Adams, Real-space refinement in PHENIX for cryo-EM and crystallography. *Acta Crystallogr. D Struct. Biol.* **74**, 531–544 (2018).
77. K. Ikeda, K. Araki, C. Takayama, Y. Inoue, T. Yagi, S. Aizawa, M. Mishina, Reduced spontaneous activity of mice defective in the epsilon 4 subunit of the NMDA receptor channel. *Brain Res. Mol. Brain Res.* **33**, 61–71 (1995).
78. R. D. Porsolt, G. Brossard, C. Hautbois, S. Roux, Rodent models of depression: Forced swimming and tail suspension behavioral despair tests in rats and mice. *Curr. Protoc. Neurosci.* **8**, doi: 10.1002/0471142301.ns0810as14 (2001).
79. N. A. Kulak, G. Pichler, I. Paron, N. Nagaraj, M. Mann, Minimal, encapsulated proteomic-sample processing applied to copy-number estimation in eukaryotic cells. *Nat. Methods* **11**, 319–324 (2014).
80. J. R. Wisniewski, A. Zougman, N. Nagaraj, M. Mann, Universal sample preparation method for proteome analysis. *Nat. Methods* **6**, 359–362 (2009).
81. E. W. Deutsch, A. Csordas, Z. Sun, A. Jarnuczak, Y. Perez-Riverol, T. Ternent, D. S. Campbell, M. Bernal-Llinares, S. Okuda, S. Kawano, R. L. Moritz, J. J. Carver, M. Wang, Y. Ishihama, N. Bandeira, H. Hermjakob, J. A. Vizcaino, The ProteomeXchange consortium in 2017: Supporting the cultural change in proteomics public data deposition. *Nucleic Acids Res.* **45**, D1100–D1106 (2017).
82. J. A. Vizcaino, A. Csordas, N. Del-Toro, J. A. Dianes, J. Griss, I. Lavidas, G. Mayer, Y. Perez-Riverol, F. Reisinger, T. Ternent, Q. W. Xu, R. Wang, H. Hermjakob, 2016 update of the PRIDE database and its related tools. *Nucleic Acids Res.* **44**, 11033 (2016).

Acknowledgments

Funding: Financial supports are gratefully acknowledged for the General National Natural Science Foundation of China (no. 31771115 and no. 31671049) to S.Z. and Y.L., respectively; The Key Program of National Natural Science Foundation of China (no. 81030065) to C.H.; STI2030 Major Projects (2022ZD0212700), the National Natural Science Foundation of China (32221003), the CAS Youth Interdisciplinary Team, the Strategic Priority Research Program of the Chinese Academy of Sciences (XDB32020000), and the Shanghai Municipal Science and Technology Major Project (2018SHZDZX05) to S.Z.; The Strategic Leading Science and Technology Project of the Chinese Academy of Sciences (XDA12040214), the "Personalized Medicines—Molecular Signature-based Drug Discovery and Development," Strategic Priority Research Program of the Chinese Academy of Sciences (XDA12040220), and The National Major Scientific and Technological Special Project for "Significant New Drugs Development" (201909301102) to Y.L.; The Science and Technology Commission of Shanghai Municipality (no. 184319071000 and no. 19140903102) to Y.L. and F.G., respectively; The Youth Program of National Natural Science Foundation of China (no. 81803828) to F.L.; and The Youth Innovation Promotion Association of Chinese Academy of Science (no. 2019280) to X.T. **Author contributions:** J.Z. and W.L. carried out whole-cell recording on *Xenopus* oocytes; J.D. and T.L. performed patch-clamp recording on HEK293T cells; L.Y. screened pharmacological targets for YY-23 on monoaminergic receptors; X.T. carried out multiplex FISH; J.Z. purified and froze the protein, collected and analyzed the cryo-EM data, and built the atomic model; J.Z., Y.H., and Y.S. validated the transgenic mice and the off target effect of CRISPR-Cas9 system; J.D., X.W., and S.R. performed slice recording; J.D. and L.Y. established the mouse model and performed the behavior tests; J.D. , Z.L. and H.Z. performed MS; C.H. and X.T. synthesized YY-23; F.L. and Y.X. performed spectroscopic analysis of YY-23; N.S. performed Western blot; X.C. generated *grin2c* KO mice; F.G., J.Z., and S.Z. wrote the manuscript; F.G. , Y.L. and S.Z. conceived the project and supervised the research. **Competing interests:** The authors declare that they have no competing interests. **Data and materials availability:** Cryo-EM density map and structural coordinate have been deposited in the Electron Microscopy Database and PDB under accession codes of EMD-38847 and 8Y1V, respectively. All data needed to evaluate the conclusions in the paper are present in the paper and/or the Supplementary Materials.

Submitted 8 May 2024
Accepted 30 January 2025
Published 5 March 2025
10.1126/sciadv.adq0444